Inorganic Chemistry
Article

Inorg. Chem. **2009**, *48*, 7765–7781 **7765**
DOI: 10.1021/ic900729d

New Family of Ferric Spin Clusters Incorporating Redox-Active *ortho*-Dioxolene Ligands

Yanyan Mulyana,[†] Ayman Nafady,[‡] Arindam Mukherjee,[†] Roland Bircher,[§] Boujemaa Moubaraki,[‡] Keith S. Murray,[‡] Alan M. Bond,[‡] Brendan F. Abrahams,[†] and Colette Boskovic*[,†]

[†]*School of Chemistry, University of Melbourne, Victoria, 3010, Australia,* [‡]*School of Chemistry, Monash University, Clayton, Victoria, 3800, Australia, and* [§]*Bragg Institute, The Australian Nuclear Science and Technology Organisation, PMB 1, Menai, New South Wales 2234, Australia*

Received April 14, 2009

Seven new di-, tri-, tetra-, and hexanuclear iron complexes that incorporate a polydentate Schiff base and variously substituted catecholate ligands have been synthesized from the trinuclear precursor $[Fe_3(OAc)_3(L)_3]$ (**1**), where LH_2 = 2-[[(2-hydroxyethyl)imino]phenylmethyl]-phenol. These were isolated as the compounds $[Fe_3(OAc)(Cat)(L)_3]$ (**2**), $[Fe_6(OAc)_2(Cat)_4(L)_4]$ (**3**), $[Fe_4(3,5\text{-}DBCat)_2(L)_4]$ (**4**), $[Bu_4N][Fe_4(OAc)(3,5\text{-}DBCat)_4(L)_2]$ (**5a**, $\mathbf{5}^-$ is the complex monoanion $[Fe_4(OAc)(3,5\text{-}DBCat)_4(L)_2]^-$), $[Fe_4(OAc)(3,5\text{-}DBCat)_3(3,5\text{-}DBSQ)(L)_2]$ (**6**), $[Fe_2(Cl_4Cat)_2(L)(LH_2)(H_2O)]$ (**7**), and $[Et_3NH]_2[Fe_2(Cl_4Cat)_2(L)_2]$ (**8a**, $\mathbf{8}^{2-}$ is the complex dianion $[Fe_2(Cl_4Cat)_2(L)_2]^{2-}$), where $CatH_2$ = catechol; 3,5-$DBCatH_2$ = 3,5-di-*tert*-butyl-catechol; 3,5-DBSQH = 3,5-di-*tert*-butyl-semiquinone, and Cl_4CatH_2 = tetrachlorocatechol. While compounds **2**−**4**, **5a**, **7**, and **8a** were obtained by directly treating **1** with the appropriate catechol, compound **6** was synthesized by chemical oxidation of **5a**. These compounds have been characterized by single crystal X-ray diffraction, infrared and UV−visible spectroscopy, voltammetry, UV−visible spectroelectrochemistry, and magnetic susceptibility and magnetization measurements. An electrochemical study of the three tetranuclear complexes (**4**, $\mathbf{5}^-$, and **6**) reveals multiple reversible redox processes due to the *o*-dioxolene ligands, in addition to reductive processes corresponding to the reduction of the iron(III) centers to iron(II). A voltammetric study of the progress of the chemical oxidation of compound **5a**, together with a spectroelectrochemical study of the analogous electrochemical oxidation, indicates that there are two isomeric forms of the one-electron oxidized product. A relatively short-lived neutral species (**5**) that possesses the same ligand arrangement as complex $\mathbf{5}^-$ is the kinetic product of both chemical and electrochemical oxidation. After several hours, this species undergoes a significant structural rearrangement to convert to complex **6**, which appears to be largely driven by the preference for the 3,5-$DBSQ^-$ ligand to bind in a non-bridging mode. Variable temperature magnetic susceptibility measurements for compounds **3**, **4**, **5a**, **6**, **7**, and **8a** reveal behavior dominated by pairwise antiferromagnetic exchange interactions, giving rise to a poorly isolated $S = 0$ ground state spin for compound **3**, well-isolated $S = 0$ ground state spins for complexes **4**, $\mathbf{5}^-$, **7** and $\mathbf{8}^{2-}$, and a well-isolated $S = 1/2$ ground state spin for complex **6**. The ground state spin values were confirmed by low temperature variable field magnetization measurements. The thermal variation of the magnetic susceptibility for compounds **3**, **4**, **5a**, **6**, **7**, and **8a** were fitted and/or simulated using the appropriate Hamiltonians to derive *J* values that are consistent with magnetostructural correlations that have been reported previously for alkoxo-bridged ferric complexes.

Introduction

The ongoing interest in iron complexes of *o*-dioxolene ligands arises in part from their relevance to several rather diverse areas in biology. For example, bacteria produce catechol-containing siderophores such as enterobactin, which is a molecule with three catechol groups linked to a trilactone backbone through amide bonds.[1] Enterobactin and other siderophores act as ligands, forming very stable chelate complexes with iron(III) centers. This provides a mechanism for bacterial iron uptake, allowing the solubilization of iron from minerals or complexed sources. In a different vein, the catechol dioxygenases are non-heme iron-containing proteins that catalyze the oxidative ring cleavage of catechol and its derivatives. There are two distinct types of these proteins: the intradiol and extradiol catechol dioxygenases, which, following the insertion of molecular oxygen into the substrate, afford muconic acids and muconic semialdehydes, respectively.[2] While the active site of the intradiol dioxygenases contains a high spin iron(III) center,

*To whom correspondence should be addressed. E-mail: c.boskovic@unimelb.edu.au.

(1) (a) Dertz, E. A.; Raymond, K. N. *Compr. Coord. Chem. II* **2004**, *8*, 141.

(2) (a) Broderick, J. B. *Essays in Biochemistry* **1999**, *34*, 173. (b) Foster, T. L.; Caradonna, J. P. *Compr Coord. Chem. II* **2004**, *8*, 343.

Published on Web 07/13/2009

the active site of the extradiol dioxygenases incorporates a high spin iron(II) center. The variation of iron oxidation state gives rise to mechanistic differences that lead to the differing regioselectivity observed for the two types of catechol dioxygenases.

An important feature of iron complexes of *o*-dioxolene ligands is that both the metal centers and the organic ligands are redox-active, which leads to multiple possible electronic states. Isoelectronic complexes can be described at either extreme as iron(III)-catecholate or iron(II)-semiquinone species, depending on the charge distribution within the molecule. A recent report of valence tautomerism in the complex $[Fe^{III}(bispicen)(Cl_4Cat)(Cl_4SQ)]$ (bispicen = *N*,*N*′-bis(2-pyridylmethyl)-1,2-ethanediamine, Cl_4CatH_2 = tetrachlorocatechol, Cl_4SQH = tetrachlorosemiquinone) is of some interest in this regard.[3] Variable temperature visible, near-infrared, and electron paramagnetic resonance (EPR) spectra of this complex in solution and in the solid state suggest a thermally induced transition to $[Fe^{II}(bispicen)(Cl_4SQ)_2]$ and a temperature-dependent equilibrium between the two tautomeric forms. Similar valence tautomeric transitions are well established for related bis(*o*-dioxolene) cobalt complexes with ancillary ligands with nitrogen donor atoms.[4] The thermodynamic favorability of these conversions is largely due to the greater vibrational and electronic entropy of the high spin cobalt(II)-containing tautomer, compared to low spin cobalt(III)-containing tautomer. Thus the cobalt(II)-containing species is favored at high temperature. However, in the case of iron it has been suggested that this entropy driver is not effective.[5] This argument is based partly on the minimal difference between Fe(II)−O and Fe(III)−O bond distances (ca. 0.03 Å) for the high spin iron centers that exist with these ligand fields, compared to the significant difference for the observed low spin Co(III)−O versus high spin Co(II)−O bond distances of about 0.2 Å. In addition, the electronic contribution to the entropy for the iron complexes is much less than for the cobalt complexes because antiferromagnetic coupling between the high spin Fe(II) center and the semiquinone ligands does not give rise to the increase in spin degeneracy that accompanies the valence tautomeric transition in the cobalt case. It is notable that the single iron complex for which a valence tautomeric transition has been reported contains tetrachlorocatecholate ligands, which have electron withdrawing chloro substituents on the catechol. This is in contrast to the cobalt complexes displaying valence tautomerism, which generally have electron-donating *tert*-butyl or similar substituents on the catecholate ligands that facilitate oxidation of the ligand to the semiquinone form.

Although numerous mononuclear iron complexes of *o*-dioxolene ligands have been investigated, only a few of examples of polynuclear complexes have been reported. These include $[Fe_2(Cat)_4(H_2O)_2]^{2-}$, $[Fe_2(Cat)_2Cl_4]^{2-}$, $[Fe_2(OAc)(Cat)_4]$, $[Fe_2(Cat)_2(L')_2]$, $[Fe(OMe)(3,6\text{-}DBSQ)_2]_2$, $[Fe_3\{(py)_2C(OH)O\}_2(3,5\text{-}DBCat)_4]^-$, $[Fe_4\{(py)_2C(OMe)O\}_2\{(Hpy)(py)C(OMe)O\}_2(3,5\text{-}DBCat)_4]^{2+}$, and $[Fe_4(3,5\text{-}DBCat)_4(3,5\text{-}DBSQ)_4]$ ($CatH_2$ = catechol; 3,5-$DBCatH_2$ = 3,5-di-*tert*-butyl-catechol; 3,5-DBSQH = 3,5-di-*tert*-butyl-semiquinone; 3,6-DBSQH = 3,6-di-*tert*-butyl-semiquinone; L′ = *N*,*N*-bis(2-pyridylmethyl)-*N*-(2-hydroxyethyl)amine).[6−12] As part of an ongoing investigation of the chemistry of polynuclear iron complexes, we have previously reported a new family of trinuclear and pentanuclear complexes of formula $[Fe_3(OAc)_3(L''_3)]$ and $[Fe_5O(OH)(OAc)_4(L'')_4]$ (H_2L'' = derivatives of salicylidene-2-ethanolamine),[13] which have proved to be excellent starting materials for the synthesis of higher nuclearity complexes. These higher nuclearity complexes were obtained by reacting the precursor tri- and pentanuclear complexes with ligands that can simultaneously chelate and bridge metal centers. Replacement of some of the acetate ligands with the new chelating/bridging ligands, together with structural rearrangement and agglomeration, has afforded novel Fe_8, Fe_{11}, and Fe_{12} species.[14] Our exploration of the potential of one such trinuclear complex $[Fe_3(OAc)_3(L)_3]$ (**1**; H_2L = 2-[[(2-hydroxyethyl)imino]phenylmethyl]-phenol), as a precursor for mixed-chelate polynuclear complexes of *o*-dioxolene ligands is reported herein. We have focused on varying the substituents of the *o*-dioxolene ligands (Chart 1) to investigate the steric effects on the structure of the resulting complexes and the electronic effects on the electronic properties and redox chemistry of the new complexes. Complexes with *o*-dioxolene ligands in the form of semiquinone radicals were a particular target to study the magnetic interactions between the metal- and ligand-based unpaired electrons.

Chart 1

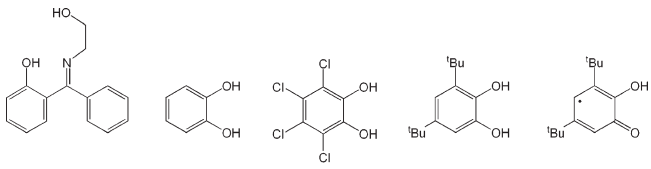

LH_2 $CatH_2$ Cl_4CatH_2 3,5-$DBCatH_2$ 3,5-DBSQH

Experimental Section

Syntheses. All manipulations were performed under aerobic conditions, using materials as received. The precursor complex **1** was prepared as described previously.[13]

$[Fe_3(OAc)(Cat)(L)_3]$ (2). A mixture of complex **1** (0.76 g, 0.72 mmol) and $CatH_2$ (0.080 g, 0.72 mmol) in MeCN (40 mL) was stirred overnight. The resulting precipitate was removed by filtration. The filtrate was evaporated to dryness on a rotary

(3) Shaikh, N.; Goswami, S.; Panja, A.; Wang, X. Y.; Gao, S.; Butcher, R. J.; Banerjee, P. *Inorg. Chem.* **2004**, *43*, 5908.
(4) (a) Hendrickson, D. N.; Pierpont, C. G. *Top. Curr. Chem.* **2004**, *234*, 63. (b) Evangelio, E.; Ruiz- Molina, D. *Eur. J. Inorg. Chem.* **2005**, 2957.
(5) Attia, A. S.; Bhattacharya, S.; Pierpont, C. G. *Inorg. Chem.* **1995**, *34*, 4427.
(6) Grillo, V. A.; Hanson, G. R.; Wang, D.; Hambley, T. W.; Gahan, L. R.; Murray, K. S.; Moubaraki, B.; Hawkins, C. J. *Inorg. Chem.* **1996**, *35*, 3568.
(7) Zirong, D.; Haltiwanger, R. C.; Bhattacharya, S.; Pierpont, C. G. *Inorg. Chem.* **1991**, *30*, 4288.
(8) Anderson, B. F.; Buckingham, D. A.; Robertson, G. B.; Webb, J.; Murray, K. S.; Clark, P. E. *Nature* **1976**, *262*, 722.
(9) Li, F.; Wang, M.; Li, P.; Zhang, T.; Sun, L. *Inorg. Chem.* **2007**, *46*, 9364.
(10) Attia, A. S.; Conklin, B. J.; Lange, C. W.; Pierpont, C. G. *Inorg. Chem.* **1996**, *35*, 1033.
(11) Boudalis, A. K.; Dahan, F.; Bousseksou, A.; Tuchagues, J. P.; Perlepes, S. P. *Dalton Trans.* **2003**, 3411.
(12) Boone, S. R.; Purser, G. H.; Chang, H. R.; Lowery, M. D.; Hendrickson, D. N.; Pierpont, C. G. *J. Am. Chem. Soc.* **1989**, *111*, 2292.
(13) (a) Boskovic, C.; Rusanov, E.; Stoeckli-Evans, H.; Güdel, H. U. *Inorg. Chem. Commun.* **2002**, *5*, 881. (b) Boskovic, C.; Labat, G.; Neels, A.; Güdel, H. U. *Dalton Trans.* **2003**, 3671. (c) Boskovic, C.; Sieber, A.; Chaboussant, G.; Güdel, H. U.; Ensling, J.; Wernsdorfer, W.; Neels, A.; Labat, G.; Stoeckli-Evans, H.; Janssen, S. *Inorg. Chem.* **2004**, *43*, 5053.
(14) Boskovic, C.; Güdel, H. U.; Labat, G.; Neels, A.; Wernsdorfer, W.; Moubaraki, B.; Murray, K. S. *Inorg. Chem.* **2005**, *44*, 3181.

evaporator and redissolved in the minimum volume of MeCN. The resulting solution was layered with Et_2O, giving a mixture of crystals of **2** and **3** after several weeks. A sample for crystallography was maintained in contact with mother liquor to prevent the loss of interstitial solvent. Although individual crystals of **2** could be isolated for single crystal studies, it was not possible to obtain a pure bulk sample for physical measurements.

[$Fe_6(OAc)_2(Cat)_4(L)_4$] (3). Solid $CatH_2$ (0.10 g, 0.91 mmol) was added to a suspension of complex **1** (0.50 g, 0.47 mmol) in CH_2Cl_2 (30 mL) and the mixture was stirred overnight. The resulting solution was filtered and layered with Et_2O, and dark purple crystals grew after 1 day. A sample for crystallography was maintained in contact with mother liquor to prevent the loss of interstitial solvent. The crystals were isolated by filtration, washed with CH_2Cl_2, then Et_2O, and vacuum-dried to afford a fully desolvated sample in 48% yield. Anal. Calcd for **3**, $C_{88}H_{74}N_4Fe_6O_{20}$: C, 57.36; H, 4.05; N, 3.04. Found: C, 57.40; H, 3.98; N, 2.97. Selected IR data (KBr, cm^{-1}): 3436 (m), 3058 (w), 2926 (w), 2857 (w), 1598 (s), 1580 (s), 1536 (s), 1476 (s), 1438 (s), 1324 (s), 1249 (s), 1028 (m), 1147 (m), 1103 (m), 1075 (m), 1037 (m), 1027 (m), 955 (w), 901 (w), 871 (m), 849 (m), 800 (m), 747 (m), 702 (m), 665 (w), 619 (s), 509 (w), 454 (w), 428 (w).

[$Fe_4(3,5\text{-}DBCat)_2(L)_4$] (4). A solution of 3,5-$DBCatH_2$ (0.195 g, 0.877 mmol) and Et_3N (0.10 mL, 1.8 mmol) in MeCN (5 mL) was added to a suspension of complex **1** (0.30 g, 0.28 mmol) in MeCN (30 mL). The mixture was then stirred at room temperature overnight, affording a green precipitate, which was filtered and washed with MeCN. Single crystals suitable for X-ray diffraction were grown by layering a CH_2Cl_2 solution of the crude product with MeCN. A sample for crystallography was maintained in contact with mother liquor to prevent the loss of interstitial solvent. The crystals were isolated by filtration, washed with CH_2Cl_2, and vacuum-dried to afford a fully desolvated sample in 30% yield. Anal. Calcd for **4**, $C_{88}H_{92}N_4Fe_4O_{12}$: C, 65.20; H, 5.72; N, 3.46. Found: C, 65.18; H, 5.81; N, 3.38. Selected IR data (KBr, cm^{-1}): 3436 (m), 2950 (m), 2863 (m), 1598 (s), 1587 (s), 1537 (s), 1464 (m), 1440 (s), 1414 (w), 1332 (s), 1245 (s), 1205 (w), 1175 (w), 1147 (m), 1120 (w), 1074 (m), 1040 (m), 1028 (m), 984 (m), 957 (w), 905 (m), 847 (m), 812 (w), 753 (m), 725 (w), 702 (m), 615 (m), 579 (m), 509 (w), 498 (w), 450 (w).

[Bu_4N][$Fe_4(OAc)(3,5\text{-}DBCat)_4(L)_2$] (5a). A solution of 3,5-$DBCatH_2$ (0.30 g, 1.3 mmol) and Et_3N (0.30 g, 2.6 mmol) in MeCN (5 mL) was added to a suspension of complex **1** (0.30 g, 0.28 mmol) in MeCN (30 mL). The mixture was then refluxed for 1 h. Excess [Bu_4N][PF_6] (1.00 g, 2.58 mmol) was added upon cooling, affording blue microcrystals. The product was then collected by filtration and washed with cold MeCN. Single crystals suitable for X-ray diffraction were obtained by layering a CH_2Cl_2 solution with hexane. A sample for crystallography was maintained in contact with mother liquor to prevent the loss of interstitial solvent. The crystals were isolated by filtration, washed with cold CH_2Cl_2 followed by hexane, and vacuum-dried to afford a fully desolvated sample in 40% yield. Anal. Calcd for **5a**, $C_{104}H_{145}N_3Fe_4O_{14}$: C, 66.28; H, 7.75; N, 2.15. Found: C, 66.28; H, 7.68; N, 2.15. Selected IR data (KBr, cm^{-1}): 3436 (m), 2950 (s), 2903 (m), 2869 (m), 1596 (s), 1554 (m), 1539 (s), 1463 (s), 1440 (s), 1415 (s), 1385 (w), 1359 (w), 1327 (m), 1279 (m), 1250 (s), 1205 (w), 1177 (w), 1145 (w), 1115 (w), 1027 (m), 987 (s), 954 (w), 900 (w) 858 (w), 832 (m), 812 (w), 754 (m), 703 (w), 685 (m), 620 (w), 577 (m), 541 (w), 508 (w), 482 (m), 455 (w).

[$Fe_4(OAc)(3,5\text{-}DBCat)_3(3,5\text{-}DBSQ)(L)_2$] (6). Solid [$Cp_2Fe$]-[$PF_6$] (0.050 g, 0.15 mmol) was added to a solution of compound **5a** (0.20 g, 0.11 mmol) in MeCN (30 mL), and the mixture was stirred for 15 h. The resulting dark blue precipitate obtained from the reaction was filtered and washed with cold MeCN. The complex was recrystallized by layering a saturated toluene solution with hexane, affording dark blue plates after several days. A sample for crystallography was maintained in contact with mother liquor to prevent the loss of interstitial solvent. The crystals were isolated by filtration, washed with hexane and vacuum-dried to afford a fully desolvated sample in 40% yield. Anal. Calcd for **6**, $C_{88}H_{109}N_2O_{14}Fe_4$: C, 64.36; H, 6.69; N, 1.71. Found: C, 64.32; H, 6.70; N, 1.70. Selected IR data (KBr, cm^{-1}): 3437 (m), 2955 (s), 2905 (m), 2868 (m), 1597 (s), 1522 (m), 1541 (s), 1492 (m), 1479 (m), 1464 (s), 1440 (s), 1413 (m), 1392 (w), 1361 (m), 1326 (m), 1280 (m), 1240 (s), 1205 (w), 1178 (w), 1154 (w), 1112 (w), 1108 (w), 1092 (w) 1027 (m), 987 (s), 953 (w), 901 (w), 859 (w), 832 (w), 754 (m), 725 (w), 702 (m), 686 (m), 655 (w), 637 (w), 618 (w), 576 (w), 556 (w), 491 (m), 454 (w), 428 (w).

[$Fe_2(Cl_4Cat)_2(L)(LH_2)(H_2O)$] (7). Solid Cl_4CatH_2 (0.30 g, 1.21 mmol) was added to a suspension of complex **1** (0.30 g, 0.28 mmol) in toluene (30 mL), and the mixture was stirred at room temperature for 1 h. The dark brown precipitate obtained from the reaction was removed by filtration and washed with toluene. Redissolution of the crude product in Et_2O, followed by slow evaporation, afforded single crystals suitable for X-ray diffraction. A sample for crystallography was maintained in contact with mother liquor to prevent the loss of interstitial solvent. The crystals were isolated by filtration, washed with cold Et_2O, and vacuum-dried to afford a fully desolvated sample in 30% yield. Anal. Calcd for **7**, $C_{42}H_{28}N_2O_9Fe_2$: C, 45.86; H, 2.57; N, 2.55. Found: C, 45.90; H, 2.48; N, 2.61. Selected IR data (KBr, cm^{-1}): 3393 (m), 3064 (m), 2947 (m), 1600 (s), 1546 (s), 1520 (m), 1485 (m), 1431 (s), 1380 (s), 1330 (m), 1290 (w), 1247 (s), 1221 (m), 1155 (m), 1122 (w), 1061 (w), 1029 (w), 989 (m), 973 (m), 897 (w), 840 (w), 809 (s), 782 (m), 759 (m), 732 (w), 700 (m), 634 (w), 615 (w), 588 (w), 567 (w), 520 (w), 466 (w), 411 (w).

[Et_3NH]$_2$[$Fe_2(Cl_4Cat)_2(L)_2$] (8a). A solution of Cl_4CatH_2 (0.45 g, 1.8 mmol) and Et_3N (0.37 g, 3.6 mmol) in MeCN (5 mL) was added to a suspension of complex **1** (0.50 g, 0.47 mmol) in MeCN (30 mL). The mixture was stirred overnight, and the resulting dark red solution was filtered. Slow evaporation of the filtrate afforded a dark brown crystalline material. Redissolution in CH_2Cl_2 and layering with Et_2O afforded single crystals suitable for X-ray diffraction. A sample for crystallography was maintained in contact with mother liquor to prevent the loss of interstitial solvent. The crystals were isolated by filtration, washed with MeCN, and vacuum-dried to afford a fully desolvated sample in 10% yield. Anal. Calcd for **8a**, $C_{54}H_{58}N_4O_8Fe_2$: C, 50.42; H, 4.54; N, 4.36. Found: C, 50.23; H, 4.51; N, 4.16. Selected IR data (KBr, cm^{-1}): 3435 (m), 1597 (m), 1536 (w), 1440 (s), 1375 (w), 1332 (w), 1246 (s), 1146 (w), 1070 (w), 968 (w), 904 (w), 846 (w), 804 (m), 780 (w), 757 (w), 702 (w), 608 (w).

X-ray Crystallography. The intensity data for compounds **2**−**4**, **5a**, and **6** were collected on a Bruker CCD diffractometer using graphite monochromated Mo Kα radiation ($\lambda = 0.71073$ Å), while the data for compounds **7** and **8a** were collected on an Oxford XCalibur diffractometer with graphite monochromated Cu Kα radiation ($\lambda = 1.54184$ Å). Crystals were transferred directly from the mother liquor to a protective oil, which was used to prevent solvent loss. A semiempirical correction for absorption was applied using the SADABS program, and analytical numerical absorption corrections were carried out using a multifaceted crystal model and the ABSPACK routine within the CrysAlis software package. The SHELXTL series of programs were used for the solution and refinement of the crystal structures. The structures were solved using direct methods and refined using a full-matrix least-squares procedure based on F^2 using all data.[15] The hydrogen atoms were placed in calculated positions and refined using a riding model. Crystallographic data for all the compounds are given in Table 1.

Magnetic Measurements. Variable temperature magnetic susceptibility and magnetization measurements were performed with a Quantum Design MPMS-5 susceptometer equipped with

(15) Sheldrick, G. M. *SHELX97 Programs for Crystal Structure Analysis*; Institut fur Anorganische Chemie der Universitat: Tammanstrasse 4, D-3400 Göttingen, Germany, 1998.

Table 1. Crystallographic Data for **2**·Et_2O, **3**·CH_2Cl_2·Et_2O, **4**·$4CH_2Cl_2$, **5a**·$5CH_2Cl_2$, **6**·$4C_7H_8$·C_6H_{14}, **7**·$4Et_2O$, and **8a**·$2CH_2Cl_2$

	2·Et_2O	**3**·CH_2Cl_2·Et_2O	**4**·$4CH_2Cl_2$	**5a**·$5CH_2Cl_2$	**6**·$4C_7H_8$·C_6H_{14}	**7**·$4Et_2O$	**8a**·$2CH_2Cl_2$
formula	$C_{57}H_{56}N_3O_4Fe_3$	$C_{93}H_{86}Cl_2Fe_6N_4O_{21}$	$C_{92}H_{100}Cl_8Fe_4N_4O_{12}$	$C_{109}H_{155}Cl_{10}Fe_4N_3O_{14}$	$C_{122}H_{155}Fe_4N_2O_{14}$	$C_{58}H_{66}N_2O_{13}Fe_2Cl_8$	$C_{56}H_{62}Cl_{12}Fe_2N_4O_8$
formula weight	1126.60	2001.66	1970.76	2309.26	2094.86	1394.43	1456.20
space group	$P\bar{1}$	$P2_1/c$	$P\bar{1}$	$P\bar{1}$	$P\bar{1}$	$P\bar{1}$	$P2_1/n$
a, Å	12.479(7)	14.215(2)	13.718(3)	17.728(2)	14.436(3)	15.510(4)	18.315(3)
b, Å	12.853(7)	33.054(5)	15.525(3)	17.743(2)	17.963(4)	15.567(4)	18.744(2)
c, Å	17.799(1)	19.978(3)	23.129(5)	19.890(2)	24.619(5)	16.177(4)	19.976(3)
α, deg	77.693(1)	90	70.600(3)	109.829(2)	92.931(4)	95.875(4)	90
β, deg	69.545(1)	104.133(4)	84.280(3)	102.394(2)	105.270(5)	106.204(5)	115.828(2)
γ, deg	85.529(1)	90	77.130(3)	90.314(2)	113.359(4)	113.366(5)	90
V, Å^3	2613.3(3)	9103(2)	4528(2)	5727(1)	5566(2)	3341(2)	6173(2)
Z	2	4	2	2	2	2	4
T, K	130	130	295	130	130	130	130
ρ_{calc}, g cm^{-3}	1.432	1.461	1.438	1.339	1.251	1.386	1.567
μ, mm^{-1}	0.886	1.063	0.926	0.789	0.573	6.913	9.013
reflns measd	16587	48163	23091	29915	29492	15174	28171
unique reflns	11452	15995	15247	19768	19357	7028	12069
$R1$, $wR2$ [$I > 2\sigma(I)$]	0.0481, 0.1177	0.0801, 0.1932	0.0781, 0.1736	0.0536, 0.1352	0.0708, 0.1520	0.0407, 0.0915	0.0705, 0.1802
$R1$, $wR2$ (all data)	0.0608, 0.1259	0.1528, 0.2201	0.1327, 0.1967	0.0720, 0.1420	0.0843, 0.1584	0.0605, 0.0971	0.0837, 0.1924

a 5 T magnet. Data were collected on powdered dried crystals, with two sets of susceptibility data collected with magnetic fields of 0.01 and 0.1 T. Pascal's constants were used to estimate the diamagnetic correction for each complex. Magnetization data were collected with fields up to 5 T and temperatures between 2.0 and 20 K.

Magnetic susceptibility data for compounds **3**, **4**, **5a**, **7**, and **8a** were fitted to the exchange Hamiltonians given in the text. The computer program MAGMUN was employed for compounds **4**, **5a**, **7**, and **8a**,[16] while the homemade computer program RBFIT was used for compound **3**. This program uses a Levenberg−Marquardt algorithm for the least-squares fit and employs full matrix diagonalization methods, making use of total spin symmetry to reduce the matrix dimensions.[17] The computer program MAGPACK was used to simulate the magnetic susceptibility data for complex **6**.[18]

Electrochemistry and Spectroelectrochemistry. Electrochemical measurements were performed in CH_2Cl_2 at 293 ± 2 K using a standard three-electrode configuration under a flow of nitrogen gas or in a Vacuum Atmospheres glovebox connected to a BASi EC Epsilon computer-controlled electrochemical workstation. The three-electrode arrangement employed for voltammetric measurements consisted of 1.0 or 1.5 mm diameter glassy carbon (Cypress) disk working electrodes, a platinum wire counter electrode, and a reference electrode consisting of a AgCl-coated Ag wire, prepared by oxidative electrolysis of the wire in 0.1 M KCl solution, separated from the analyte solution by a glass frit of low porosity containing the same solvent/supporting electrolyte mixture. For bulk electrolysis experiments, large platinum gauze and platinum mesh baskets were used as the working electrode and counter electrode, respectively. The Ag/AgCl reference electrode was the same as that employed in the voltammetric studies. Analyte solutions of 1 to 3 mM were prepared in CH_2Cl_2 containing either 0.1 M [Bu_4N][PF_6] or 0.05 M [Bu_4N][$B(C_6F_5)_4$] as the supporting electrolyte.

All potentials reported in this paper are in volt versus the ferrocene/ferrocenium redox couple. This was achieved by addition of decamethylferrocene as an internal standard and then calibrated to the ferrocene/ferrocenium potential scale by addition of −0.61 V (in CH_2Cl_2 with 0.05 M [Bu_4N][$B(C_6F_5)_4$]) or −0.55 V (in CH_2Cl_2 with 0.1 M [Bu_4N][PF_6]).[19] Mechanistic aspects of the voltammetric processes were investigated by applying the appropriate diagnostic criteria to cyclic voltammetric data as described elsewhere.[20]

UV−visible spectroelectrochemistry was performed using a homemade Optically Transparent Thin-Layer Electrolysis (OTTLE) cell with platinum gauze as the working electrode. The experiments employed approximately 2 mL of CH_2Cl_2 solutions containing 0.1 M [Bu_4N][PF_6] and 0.2−0.75 mM analyte. The UV−visible spectra were recorded with a Varian Cary 5000 spectrophotometer.

Other Measurements. Infrared spectra (KBr disk) were recorded on a BioRad 175 FTIR spectrometer. UV−visible spectra were measured on a Varian Cary 50 Bio UV−visible Spectrophotometer. Elemental analyses were performed at Chemical and Microanalytical Services, Belmont, Victoria, Australia.

Results and Discussion

Syntheses. Complex **1** proved to be an excellent starting material for the synthesis of new polynuclear ferric complexes containing substituted catecholate ligands. The formation of these new complexes from the reaction of **1** with the deprotonated or acid forms of the catechol proligands involves the concerted loss of acetate ligands, coordination of catecholate ligands, and structural rearrangement. The variety of products isolated suggests that a range of species are present in equilibrium in solution, with the relative solubilities in the particular solvent system governing the identity of the species that crystallizes from solution. Most of the products obtained were isolated in reasonable yield. The pathways for the syntheses of all of the compounds are summarized in Scheme 1.

The reaction of complex **1** with approximately 1 equiv of catechol in acetonitrile afforded a significant quantity of precipitate and a dark red solution. Following removal of the precipitate, evaporation of the mother liquor to dryness, redissolution in acetonitrile, and layering with

(16) Thompson, L. K.; Waldmann, O.; Xu, Z. *Coord. Chem. Rev.* **2005**, *249*, 2677.
(17) (a) Gatteschi, D.; Pardi, L. *Gazz. Chim. Ital.* **1993**, *123*, 231. (b) Waldmann, O. *Phys. Rev. B* **2000**, *61*, 6138.
(18) Borrás-Almenar, J. J.; Clemente-Juan, J. M.; Coronado, E.; Tsukerblatt, B. S. *MAGPACK; Inorg. Chem.* **1999**, *38*, 6081.
(19) Barrire, F.; Geiger, W. E. *J. Am. Chem. Soc.* **2006**, *128*, 3980.
(20) Geiger, W. E. In *Laboratory Techniques in Electrochemistry*, 2nd ed.; Kissinger, P. T., Heineman, W. R., Eds.; Marcel Dekker: New York, 1996; Chapter 23.

Scheme 1

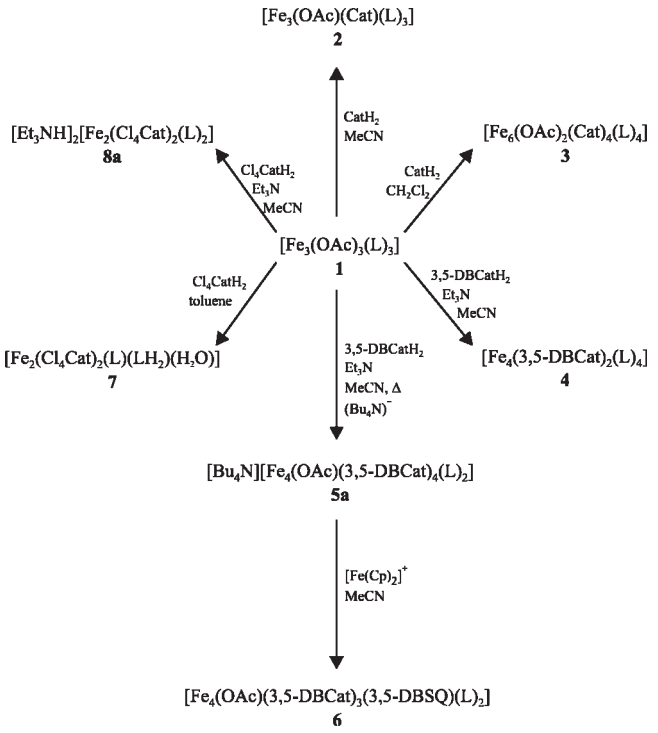

diethyl ether, a mixture of crystals of complexes **2** and **3** were obtained. Redissolution of the original precipitate in dichloromethane and layering with diethyl ether gave a mixture of crystalline complex **2** and an amorphous material. Although individual crystals of the trinuclear complex **2** could be isolated for X-ray crystallography, it was not possible to obtain the pure bulk sample required for physical measurements. In contrast, repeating the original reaction in dichloromethane and layering the resulting purple solution with diethyl ether afforded a pure crystalline sample of the hexanuclear complex **3**, with an improved yield obtained when 2 equiv of catechol were employed. The formation of complexes **2** and **3** are summarized in eqs 1 and 2, respectively.

$$\underset{\mathbf{1}}{[Fe_3(OAc)_3(L)_3]} + CatH_2 \rightarrow \underset{\mathbf{2}}{[Fe_3(OAc)(Cat)(L)_3]} + 2\,AcOH \quad (1)$$

$$2\,\underset{\mathbf{1}}{[Fe_3(OAc)_3(L)_3]} + 4\,CatH_2 \rightarrow \underset{\mathbf{3}}{[Fe_6(OAc)_2(Cat)_4(L)_4]} + 4\,AcOH + 2\,LH_2 \quad (2)$$

Although a pure crystalline sample of **3** could be obtained from the initial crystallization from dichloromethane and ether, subsequent attempts to recrystallize this material from the same solvent mix yielded a microcrystalline material that appeared to be a mixture of **2** and **3** according to elemental analysis data. This suggests that in the absence of excess acetic acid, complex **3** is unstable in solution, partially degrading to complex **2**.

The reaction in acetonitrile of complex **1** with excess 3,5-di-*tert*-butyl-catechol under basic conditions resulting from the addition of triethylamine gave different products depending on the temperature of the reaction. When undertaken at ambient temperature, the resulting green precipitate could be recrystallized from dichloromethane/acetonitrile to give the neutral tetranuclear complex **4** in good yield. When the solution was refluxed and allowed to cool, addition of tetrabutylammonium hexafluorophosphate to the resulting dark blue solution afforded a microcrystalline blue product that could be recrystallized from dichloromethane/hexane to give compound **5a**, which is the tetrabutylammonium salt of a monoanionic tetranuclear complex ($\mathbf{5}^-$). The formation of complexes **4** and $\mathbf{5}^-$ are summarized in eqs 3 and 4, respectively.

$$4\,\underset{\mathbf{1}}{[Fe_3(OAc)_3(L)_3]} + 6\,(3,5\text{-}DBCat)^{2-} \rightarrow \underset{\mathbf{4}}{3\,[Fe_4(3,5\text{-}DBCat)_2(L)_4]} + 12\,AcO^- \quad (3)$$

$$4\,\underset{\mathbf{1}}{[Fe_3(OAc)_3(L)_3]} + 12\,(3,5\text{-}DBCat)^{2-} \rightarrow \underset{\mathbf{5^-}}{3\,[Fe_4(OAc)(3,5\text{-}DBCat)_4(L)_2]^-} + 6\,L^{2-} + 9\,AcO^- \quad (4)$$

The reversible potential (−0.27 V versus ferrocene/ferrocenium, vide infra) for the first one-electron oxidation process of $\mathbf{5}^-$ suggested that this process might be readily accessible by chemical oxidation. The reaction of a solution of **5a** in acetonitrile with 1.4 equiv of ferrocenium hexafluorophosphate afforded a blue precipitate that could be recrystallized from toluene/hexane to give **6** in 40% yield according to eq 5.

$$\underset{\mathbf{5^-}}{[Fe_4(OAc)(3,5\text{-}DBCat)_4(L)_2]^-} + [Cp_2Fe]^+ \rightarrow \underset{\mathbf{6}}{[Fe_4(OAc)(3,5\text{-}DBCat)_3(3,5\text{-}DBSQ)(L)_2]} + [Cp_2Fe] \quad (5)$$

Varying the amount of ferrocenium hexafluorophosphate employed in the reaction did not improve the yield of **6**.

The reaction of a suspension of complex **1** and tetrachlorocatechol in toluene or dichloromethane afforded a brown precipitate that could be recrystallized from diethyl ether to give complex **7**. The reaction of complex **1** with tetrachlorocatechol and triethylamine in acetonitrile gave a clear solution. The residue that was obtained following the evaporation of this solution to dryness was recrystallized from dichloromethane/ether to give compound **8a**, which is the triethylammonium salt of the dianionic dinuclear complex ($\mathbf{8}^{2-}$). The formation of

complexes **7** and $\mathbf{8}^{2-}$ are summarized in eqs 6 and 7, respectively.

$$2\,[Fe_3(OAc)_3(L)_3] + 6\,Cl_4CatH_2 + 3\,H_2O \rightarrow \underset{\mathbf{1}}{} \qquad 3\,[Fe_2(Cl_4Cat)_2(L)(LH_2)(H_2O)] + 6\,AcOH \quad (6)$$

$$\underset{\mathbf{7}}{}$$

$$2\,[Fe_3(OAc)_3(L)_3] + 6\,Cl_4Cat^{2-} \rightarrow \underset{\mathbf{1}}{} \qquad 3\,[Fe_2(Cl_4Cat)_2(L)_2]^{2-} + 6\,AcO^- \quad (7)$$

$$\underset{\mathbf{8}^{2-}}{}$$

The direct substitution of tetrachlorocatechol with tetrabromocatechol in each of these reactions afforded microcrystalline materials that were not suitable for X-ray diffraction and which proved to be more insoluble in dichloromethane than the chlorinated analogues.

Dianionic catecholate ligands are evident in all of the complexes synthesized directly from the trinuclear precursor **1**, regardless of whether the catechol precursor was deliberately deprotonated prior to reaction with **1**. However, the relatively electron donating *tert*-butyl substituents of 3,5-di-*tert*-butyl-catechol render this species the weakest acid of the three catechol proligands, and it was found that, in contrast to the other two catechols employed, protonated 3,5-di-*tert*-butyl-catechol did not react with the precursor complex **1** until base was added to the solution.

Vacuum drying the isolated crystalline products afforded fully desolvated samples in all cases. The purity of bulk samples of compounds **3**, **4**, **5a**, **6**, **7**, and **8a** for physical measurements was established by elemental analysis.

Structures. Labeled structural diagrams of the complexes of interest are presented in Figures 1 (**2** and **3**), 2 (**4**, $\mathbf{5}^-$ and **6**), and 3 (**7** and $\mathbf{8}^{2-}$), while the different binding modes displayed by the ligands are depicted in Figure 4. The most relevant interatomic distances and angles are available in Tables 2−5. All of the iron centers in the complexes are six coordinate with distorted octahedral coordination geometry and bond valence sum calculations indicating that they are all Fe(III).[21]

Complex **2** crystallizes in the triclinic space group $P\bar{1}$, with one neutral trinuclear complex (Figure 1a) in the asymmetric unit. This asymmetric complex contains a $\{Fe^{III}_3(\mu_3\text{-O})(\mu_2\text{-O})_3\}^+$ core unit, where the μ_3-O atom is from the ethoxo arm of a μ_3-L^{2-} (Figure 4), two of the μ_2-O atoms are from the ethoxo arms of two μ_2-L^{2-} ligands, and the remaining μ_2-O atom is a phenoxo-type oxygen atom from the μ_2-Cat^{2-} ligand. The structure of the core can be described as a monovacant distorted cubane. The remaining coordination sites of the iron centers are occupied by the L^{2-} and Cat^{2-} ligands, in addition to a single acetate ligand that binds in the common syn,syn μ_2-mode. The structural differences between complex **2** and the precursor trinuclear complex

(21) Brese, N. E.; O′ Keefe, M. *Acta Crystallogr.* **1991**, *B47*, 192.

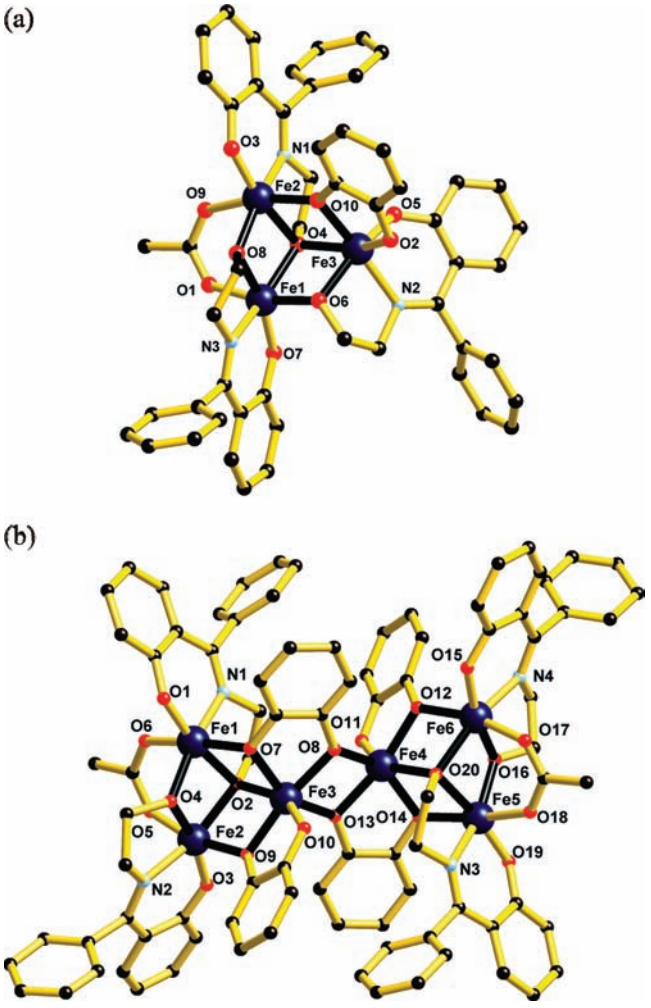

Figure 1. Structural representation of (a) complex **2** and (b) complex **3**. Color code: Fe (dark blue), O (red), N (light blue), C (black). Hydrogen atoms are omitted for clarity.

1 arise from the μ_3-O_{alkoxo} atom that is present in **2** but not in **1** and the single bridging acetate ligand in **2** as opposed to the three bridging acetate ligands in **1**.

Complex **3** crystallizes in the monoclinic $P2_1/c$ space group with one neutral hexanuclear complex (Figure 1b) in the asymmetric unit. The $\{Fe^{III}_6(\mu_3\text{-O})_2(\mu_2\text{-O})_8\}^{2-}$ core of **3** resembles two of the core units of complex **2** linked by two μ_2-$O_{phenoxo}$ atoms from two μ_3-Cat^{2-} ligands. Although this complex is strictly asymmetric, it has an approximate inversion center. The two planes defined by the three iron centers in each half of the molecule (Fe1, Fe2 and Fe3; Fe4, Fe5 and Fe6) are nearly parallel, with a dihedral angle of 6.81(4)°. The iron coordination is completed by two μ_2-Cat^{2-} ligands, two μ_3-L^{2-} ligands, two μ_2-L^{2-} ligands and two μ_2-acetate ligands.

Complex **4** crystallizes in the triclinic space group $P\bar{1}$, such that the unit cell contains two independent molecules of complex **4**, each of which lies on a center of inversion (Figure 2a). Although the two molecules are crystallographically distinct they are chemically similar, with identical connectivities and ligand binding modes. Each neutral tetranuclear complex has an $\{Fe^{III}_4(\mu_3\text{-O})_2(\mu_2\text{-O})_4\}$ core that can be described as a divacant face-shared distorted double cubane unit, where the individual

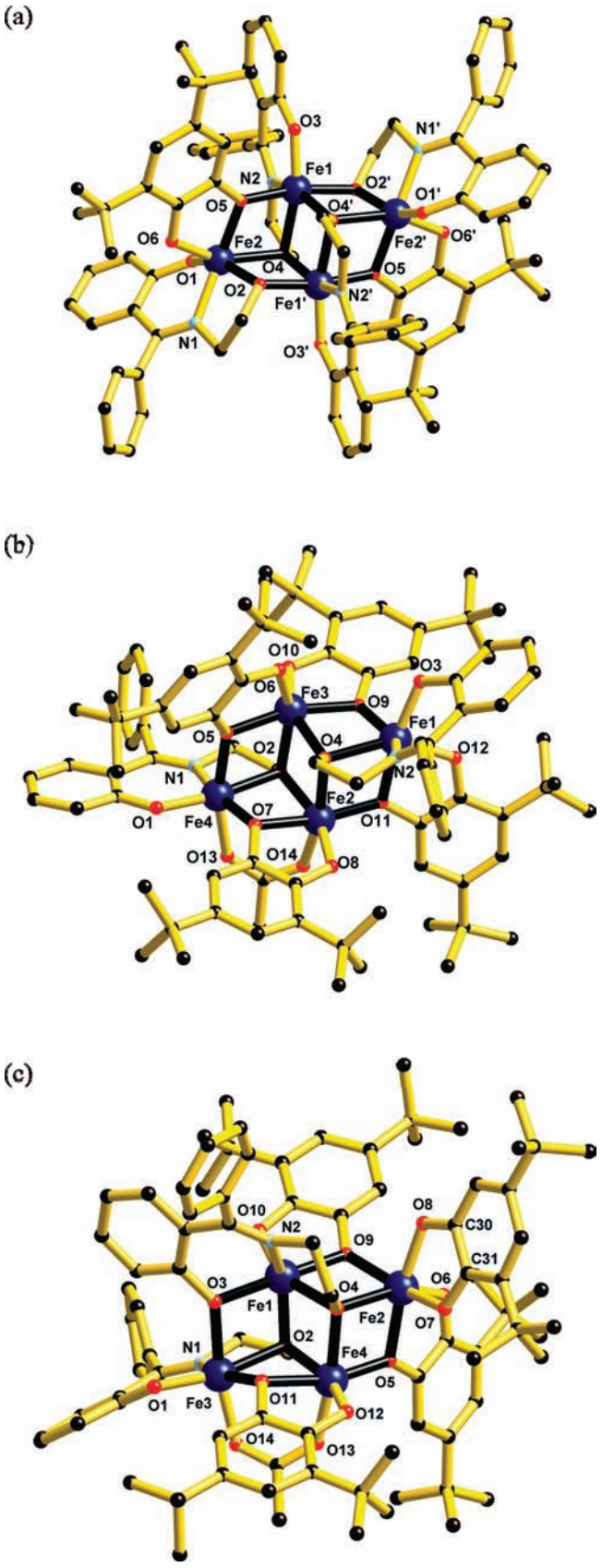

Figure 2. Structural representation of (a) one of the independent molecules of complex **4**, (b) complex $\mathbf{5}^{-}$, and (c) complex **6**. Color code as in Figure 1.

monovacant cubane units are similar to the core of complex **2**. The four iron centers of this centrosymmetric

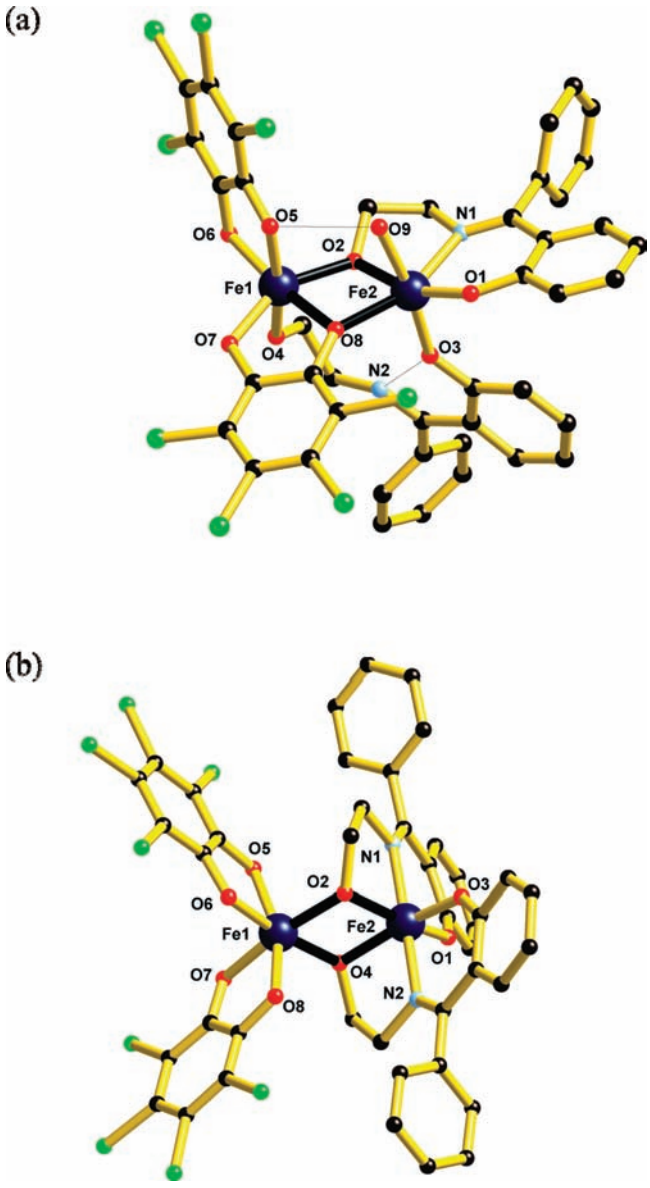

Figure 3. Structural representation of (a) complex **7** and (b) complex $\mathbf{8}^{2-}$. Color code as in Figure 1 with Cl (green); the dashed lines indicate intramolecular hydrogen bonds.

complex are coplanar. The two μ_3-O atoms in the core are from the ethoxo arms of μ_3-L^{2-} ligands, two of the μ_2-O atoms are from the ethoxo arms of μ_2-L^{2-} ligands and the remaining two μ_2-O atoms are phenoxo-type oxygen atoms from the two μ_2-3,5-$DBCat^{2-}$ ligands. The main conformational differences between the two crystallographically independent molecules of complex **4** arise from different orientations of the ligands, particularly the phenyl groups.

Compound **5a** crystallizes in the triclinic space group $P\bar{1}$, with one monoanionic tetranuclear complex ($\mathbf{5}^{-}$) in the asymmetric unit (Figure 2b). The $\{Fe^{III}_4(\mu_3\text{-}O)_2(\mu_2\text{-}O)_4\}$ core of complex $\mathbf{5}^{-}$ is similar to that of complex **4**, although the four iron centers of this asymmetric complex are only approximately coplanar. As in **4**, the two μ_3-O atoms in the core of $\mathbf{5}^{-}$ are from the ethoxo arms of two μ_3-L^{2-} ligands; however, the four μ_2-O atoms in the core of $\mathbf{5}^{-}$ are all phenoxo-type oxygen atoms from the four μ_2-3,5-$DBCat^{2-}$ ligands. Although the core topologies of the

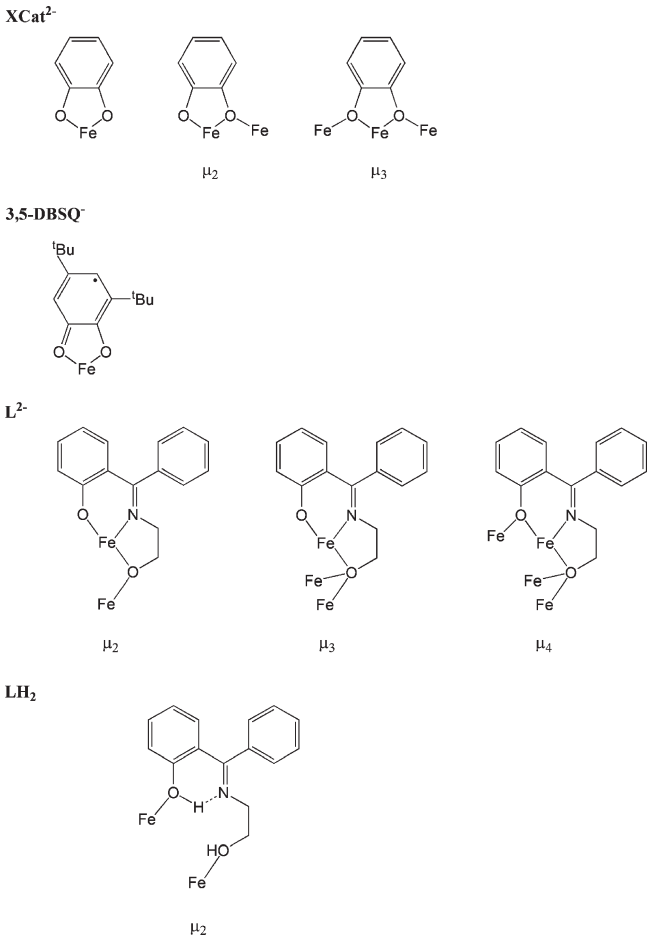

Figure 4. Ligand binding modes in the complexes.

Table 2. Fe−O Distances (Å) for Compounds **2**·Et_2O, **3**·CH_2Cl_2·Et_2O, **4**·4CH_2Cl_2, **5a**·5CH_2Cl_2, **6**·4C_7H_8·C_6H_{14}, **7**·4Et_2O, and **8a**·2CH_2Cl_2.[a]

compound	Fe−O (μ_2-OR)	Fe−O (μ_3-OR)
2·Et_2O	1.966(2)−2.049(2)	2.112(2)−2.186(2)
3·CH_2Cl_2·Et_2O	1.935(4)−2.040(5)	2.088(5)−2.159(5)
4·4CH_2Cl_2	1.966(4)−2.069(4)	2.083(4)−2.238(4)
5a·5CH_2Cl_2	1.920(2)−2.065(2)	2.079(2)−2.183(3)
6·4C_7H_8·C_6H_{14}	1.932(3)−2.079(3)	2.051(3)−2.173(3)
7·4Et_2O	1.977(3)−2.093(3)	
8a·2CH_2Cl_2	2.012(3)−2.022(3)	

[a] Distances to bridging O atoms only.

two complexes are similar, the structural differences arise from the different ligand combinations in the two complexes, with four L^{2-} and two 3,5-DBcat^{2-} ligands in **4**, versus two L^{2-} and four 3,5-DBCat^{2-} ligands in $\mathbf{5}^-$. Complex $\mathbf{5}^-$ also possesses a single μ_2-acetate ligand bridging Fe2 and Fe4.

Complex **6** crystallizes in the triclinic $P\bar{1}$ space group with one neutral tetranuclear complex (Figure 2c) in the asymmetric unit. Although the first one-electron oxidation of $\mathbf{5}^-$ is chemically reversible on the voltammetric time scale (vide infra), interesting structural rearrangements occur following the formation of **6** from chemical oxidation of **5a**. Like **4** and $\mathbf{5}^-$, **6** possesses a $\{Fe^{III}_4(\mu_3\text{-}O)_2(\mu_2\text{-}O)_4\}$ core with approximately coplanar iron centers. The two μ_3-O atoms are again ethoxo type from the two L^{2-} ligands, three of the μ_2-O atoms are from the three μ_2-3,5-DBCat^{2-} ligands, while the fourth μ_2-O atom is from one of the L^{2-} ligands that binds overall in an unusual μ_4-mode (Figure 4). Complex **6** is the only complex in this study to display this binding mode for L^{2-}. In the simplest sense the structural rearrangement that occurs during the formation of **6** from $\mathbf{5}^-$ involves one of the L^{2-} ligands (the one that contains atom N2) and one of the *o*-dioxolene ligands (defined by O5 and O6 in $\mathbf{5}^-$ and O7 and O8 in **6**) exchanging binding sites, while the coordination of the remaining ligands does not change. The ligands that change their binding positions also change their binding modes with the μ_3-mode of L^{2-} in $\mathbf{5}^-$ converting to a μ_4-mode in **6**, while the μ_2-bridging 3,5-DBCat^{2-} ligand in $\mathbf{5}^-$ converts to a chelating-only 3,5-DBSQ$^-$ ligand in **6**. This structural rearrangement involves breaking and reforming five Fe−O and Fe−N bonds. These rearrangements are likely associated with the lower affinity of the single 3,5-DBSQ$^-$ ligand to bridge Fe centers, consistent with the relatively electron poor nature of the 3,5-DBSQ$^-$ ligand compared to the 3,5-DBCat^{2-} form. This 3,5-DBSQ$^-$ ligand is readily distinguished (vide infra) from the three 3,5-DBCat^{2-} ligands crystallographically by the short C−O and long ring (O)C−C(O) bond lengths (Table 5).

Complex **7** crystallizes in the triclinic space group $P\bar{1}$, with one neutral dinuclear complex (Figure 3a) in the asymmetric unit. This complex is asymmetric with both Cl_4Cat^{2-} ligands chelating one iron center and the L^{2-} and LH_2 ligands chelating the other iron center. The molecule has a $\{Fe^{III}_2(\mu_2\text{-}O)_2\}^{2+}$ core, with one of the core oxygen atoms from the ethoxo arm of the μ_2-L^{2-} ligand and the other a phenoxo-type oxygen atom from a μ_2-Cl_4Cat^{2-} ligand. With the other Cl_4Cat^{2-} ligand binding only in a chelating manner, the two Cl_4Cat^{2-} ligands bind in two different modes in this complex. Complex **7** is the only species in this study to incorporate a protonated form of the Schiff base ligand LH_2, which acts as a μ_2-bridging ligand (Figure 4), in addition to the μ_2-bridging L^{2-}. The C−N bond length for the bound LH_2 ligand is 1.304(8) Å, which is close to the 1.296(8) Å observed for the L^{2-} ligand and consistent with the maintenance of imine character, rather than reduction to an amine. The unusual binding mode of LH_2 is coincident with an intramolecular hydrogen bond between the imine fragment and the phenolic oxygen atom, with a O−H···N distance of 2.55 Å. Another intramolecular hydrogen bond is evident between the catecholate oxygen atom O5 bound to Fe1 and O9 of the terminal water ligand bound to Fe2, with an O−H···O separation of 2.66 Å.

Compound **8a** crystallizes in the monoclinic space group $P2_1/n$ with one dianionic dinuclear complex ($\mathbf{8}^{2-}$) in the asymmetric unit (Figure 3b). As occurs in complex **7**, both Cl_4Cat^{2-} ligands chelate one iron center, while the L^{2-} ligands both chelate the other iron center. Complex $\mathbf{8}^{2-}$ also features a $\{Fe^{III}_2(\mu_2\text{-}O)_2\}^{2+}$ core; however, in this case both bridging oxygen atoms are from the ethoxo arms of the two μ_2-L^{2-} ligands. Complex $\mathbf{8}^{2-}$ is the only species in the present study in which none of the $XCat^{2-}$ ligands bridge metal centers. Although the dianion is strictly asymmetric, it has approximate C_2 symmetry, with the C_2 axis lying along the iron−iron vector.

Table 3. Fe···Fe Distances (Å) for Compounds **2**·Et_2O, **3**·CH_2Cl_2·Et_2O, **4**·$4CH_2Cl_2$, **5a**·$5CH_2Cl_2$, **6**·$4C_7H_8$·C_6H_{14}, **7**·$4Et_2O$, and **8a**·$2CH_2Cl_2$

compound	via $(\mu_2\text{-OR})_2$	via $(\mu_2\text{-OR})(\mu_3\text{-OR})$	via $(\mu_3\text{-OR})_2$	via $(\mu_2\text{-OR})(\mu_3\text{-OR})(\mu_2\text{-OAc})$
2·Et_2O		3.266(6)−3.307(5)		3.058(6)
3·CH_2Cl_2·Et_2O	3.206(1)	3.219(1)−3.267(1)		3.075(2)−3.084(1)
4·$4CH_2Cl_2$		3.253(2)−3.297(2)	3.172(2)−3.212(2)	
5a·$5CH_2Cl_2$		3.293(7)−3.310(8)	3.305(9)	3.086(7)
6·$4C_7H_8$·C_6H_{14}		3.205(8)−3.294(1)	3.206(1)	3.165(1)
7·$4Et_2O$	3.227(1)			
8a·$2CH_2Cl_2$	3.185(1)			

Table 4. Fe−O−Fe Bridging Angles (deg) for Compounds **2**·Et_2O, **3**·CH_2Cl_2·Et_2O, **4**·$4CH_2Cl_2$, **5a**·$5CH_2Cl_2$, **6**·$4C_7H_8$·C_6H_{14}, **7**·$4Et_2O$, and **8a**·$2CH_2Cl_2$

compound	via μ_2-OR	via μ_3-OR
2·Et_2O	100.29(8)−110.02(9)	91.98(7)−99.74(7)
3·CH_2Cl_2·Et_2O	101.8(2)−109.3(2)	92.8(2)−100.4(2)
4·$4CH_2Cl_2$	108.8(2)−110.8(2)	97.6(2)−99.2(2)
5a·$5CH_2Cl_2$	100.27(9)−111.0(1)	92.99(8)−103.53(9)
6·$4C_7H_8$·C_6H_{14}	102.6(1)−111.0(1)	99.6(1)−101.1(1)
7·$4Et_2O$	102.2(1)−107.5(1)	
8a·$2CH_2Cl_2$	104.0(1)−104.5(1)	

The C−O and ring (O)C−C(O) bond distances are generally considered diagnostic for the oxidation state of *o*-dioxolene ligands.[11,12,22] Catecholate C−O distances are typically in the range 1.33−1.39 Å, semiquinone C−O distances are in the range 1.27−1.31 Å, and quinone C−O distances are usually around 1.23 Å. These ranges encompass the different binding modes of the ligands, with longer C−O distances observed for an oxygen atom that bridges two metal centers. The ring (O)C−C(O) distances are also informative, with distances in the range 1.36−1.44 Å for catecholates, in the range 1.45−1.48 Å for semiquinones and around 1.5 Å for quinones. With the exception of the single 3,5-$DBSQ^-$ ligand in complex **6**, which has C−O and ring (O)C−C(O) bond distances consistent with a semiquinone, all of the *o*-dioxolene ligands in complexes **2**−**4**, $\mathbf{5}^-$, **6**, **7**, and $\mathbf{8}^{2-}$ display C−O and ring (O)C−C(O) distances that lie within the ranges typical for catecholate ligands (Table 5).

The coordinative versatility of the ligands used in this work (Figure 4) gives rise to the multiple structural types evident in the present complexes. The structural differences between the products obtained following the reaction of the same trinuclear precursor complex **1** with the different catechol species can be rationalized in part by a consideration of both electronic and steric effects of the catechol substituents. The relatively electron withdrawing chloro substituents render Cl_4Cat^{2-} the least likely of the three $XCat^{2-}$ ligands to bridge iron centers and the most likely to simply chelate, giving rise to relatively simple dinuclear complexes. On the other hand Cat^{2-} and 3,5-$DBCat^{2-}$ are more readily able to bridge the metal centers, and the monovacant distorted cubane structural fragment that is evident in complexes, **2**, **3**, **4**, $\mathbf{5}^-$, and **6** is the result. The metric parameters associated with these units across the four complexes that incorporate them are very similar (Tables 3−5). These structural units are linked indirectly in complex **3** and directly through face-sharing in complexes **4**, $\mathbf{5}^-$, and **6**. It seems likely that the steric bulk associated with the *tert*-butyl substituents has limited to four the nuclearity of the complexes obtained from 3,5-$DBCat^{2-}$. This nuclearity limitation is also evident in the previously reported tetranuclear complex [Fe_4(3,5-DBCat)$_4$(3,5-DBSQ)$_4$], which contains a $\{Fe^{III}{}_4(\mu_3\text{-O})_2(\mu_2\text{-O})_4\}$ core similar to those of **4** and $\mathbf{5}^-$.[12] Although the binding modes of the 3,5-$DBCat^{2-}$ and 3,5-$DBSQ^-$ ligands in [Fe_4(3,5-DBCat)$_4$-(3,5-DBSQ)$_4$] and in the present complexes differ, the semiquinone form of the ligand clearly shows a lower affinity than the catecholate form for bridging Fe centers in both complex **6** and [Fe_4(3,5-DBCat)$_4$(3,5-DBSQ)$_4$]. The structures of the dinuclear complexes **7** and **8a** may also be compared with those of the two previously reported dinuclear ferric complexes of catechol.[6−9] Although a $\{Fe^{III}{}_2(\mu_2\text{-O})_2\}^{2+}$ core is common to all, the complexes $[Fe_2(Cat)_4(H_2O)_2]^{2-}$, $[Fe_2(Cat)_2Cl_4]^{2-}$, and $[Fe_2(OAc)(Cat)_4]$ have both of the core oxygen atoms provided by two μ_2-catechol ligands,[6−8] while **7** has one of the core oxygen atoms provided by a Cl_4Cat^{2-}, and $\mathbf{8}^{2-}$ and $[Fe_2(Cat)_2(L')_2]$ both have the two core oxygen atoms provided by ancillary ligands.[9]

Infrared Spectroscopy. Infrared spectra for compounds **3**, **4**, **5a**, **6**, **7**, and **8a** were obtained in the range 400−4000 cm^{-1} from pressed KBr disks. The infrared spectra of all the compounds display medium to strong bands in the two regions 1237−1280 and 1400−1500 cm^{-1} which are typical for metal-catecholate complexes.[6,23] The infrared spectra of **5a** and its one-electron oxidized derivative **6** are very similar (Supporting Information, Figure S1). However, the bands at 1479 and 1492 cm^{-1} in the spectrum of **6** that are absent in that of **5a** may be assigned to the C−O semiquinone stretch of the 3,5-$DBSQ^-$ ligand.[24] All of the compounds also display a band at around 1590−1600 cm^{-1} that is characteristic of the C=N stretch for the iron-coordinated imine moiety in ligand L^{2-}.[25] The spectrum of complex **7** displays a very broadband with ill-defined features between 3000 and 3700 cm^{-1} that is not apparent in the spectra of the other compounds. This is likely due to the O−H and N−H stretches of the protonated LH_2 ligand.

UV−visible Spectroscopy. UV−visible spectra were measured for solutions of compounds **4**, **5a**, **6**, **7**, and **8a** in dichloromethane between 250 and 1100 nm (Table 6). Spectra were also obtained in acetonitrile for the compounds that were soluble (**5a**, **6**, and **7**). Monitoring the spectra of the solutions over time indicated that compounds **4**, **5a**, **6**, **7**, and **8a** were all stable in solution for at

(22) Ding, Z.; Bhattacharya, S.; McCusker, J. K.; Hagen, P. M.; Hendrickson, D. N.; Pierpont, C. G. *Inorg. Chem.* **1992**, *31*, 870.

(23) Lynch, M. W.; Valentine, M.; Hendrickson, D. N. *J. Am. Chem. Soc.* **1982**, *104*, 6982.

(24) Pecoraro, V. L.; Harris, W. R.; Wong, G. B.; Carrano, C. J.; Raymond, K. N. *J. Am. Chem. Soc.* **1983**, *105*, 4623.

(25) (a) Champouret, Y. D. M.; Maréchal, J. D.; Chaggar, R. K.; Fawcett, J.; Kuldip Singh, K.; Maseras, F.; Solan, G. A. *New. J. Chem.* **2007**, *31*, 75. (b) Sharma, V. K.; Srivastava, S. *J. Coord. Chem.* **2008**, *61*, 178.

Table 5. Average C−O and Ring (O)C−C(O) Distances (Å) of the Cat^{2-}, Cl_4Cat^{2-}, 3,5-$DBCat^{2-}$, and 3,5-$DBSQ^{-}$ Ligands in Compounds **2**·Et_2O, **3**·CH_2Cl_2·Et_2O, **4**·$4CH_2Cl_2$, **5a**·$5CH_2Cl_2$, **6**·$4C_7H_8$·C_6H_{14}, **7**·$4Et_2O$, and **8a**·$2CH_2Cl_2$

	C−O			ring (O)C−C(O)	
compound	$XCat^{2-}$ terminal O	μ_2-O	3,5-$DBSQ^{2-}$	$XCat^{2-}$	3,5-$DBSQ^{2-}$
2·Et_2O	1.343(3)	1.368(3)		1.409(4)	
3·CH_2Cl_2·Et_2O	1.322(9)−1.349(8)	1.333(8)−1.373(8)		1.36(1)−1.397(9)	
4·$4CH_2Cl_2$	1.329(7)−1.345(7)	1.370(7)−1.376(7)		1.406(8)−1.415(8)	
5a·$5CH_2Cl_2$	1.335(4)−1.357(4)	1.352(4)−1.370(4)		1.403(4)−1.415(4)	
6·$4C_7H_8$·C_6H_{14}	1.341(5)−1.354(5)	1.350(5)−1.361(4)	1.287(5)−1.291(5)	1.396(5)−1.410(6)	1.450(6)
7·$4Et_2O$	1.332(5)−1.341(5)	1.336(5)		1.420(6)−1.424(6)	
8a·$2CH_2Cl_2$	1.311(6)−1.329(5)			1.428(6)−1.438(6)	

Table 6. UV-visible Spectral Data for Compounds **4**, **5a**, **6**, **7**, and **8a** in Dichloromethane and Acetonitrile

compound	solvent	λ_{max}, nm ($\varepsilon \times 10^3$, M^{-1} cm^{-1})
4	MeCN	insoluble
	CH_2Cl_2	288[a] (36.5), 543 (7.97)
5a	MeCN	284 (36.1), 319[a] (21.0), 607 (12.3)
	CH_2Cl_2	285 (40.6), 420[a] (14.0), 600 (15.4)
6	MeCN	283[a] (31.0), 651 (9.34)
	CH_2Cl_2	286[a] (38.6), 618 (13.2)
7	MeCN	294 (17.5), 551 (5.05)
	CH_2Cl_2	289[a] (21.6), 549 (5.40)
8	MeCN	303 (26.1), 489 (8.36)
	CH_2Cl_2	303 (24.9), 489 (5.78)

[a] Shoulder.

least a period of several hours. Two intense bands are evident for each of the compounds, with a less intense band in the visible region in the range 489−651 nm and more intense band in the UV region between 280 and 320 nm, which occurs in some cases as a shoulder on an even more intense absorption. A slight solvent-dependence is observed for both of these bands. The UV band has been assigned previously as an internal transition within the *o*-dioxolene ligands,[26] while the band in the visible region has been attributed to a ligand-to-metal charge transfer (LMCT) from the catecholate ligands to the Fe(III) center, that is, Fe(III)-Cat → Fe(II)-SQ.[5,27] The energy of this LMCT band varies somewhat between the complexes, reflecting the varying Lewis basicities of the differently substituted catecholate ligands.

Electrochemistry and Spectroelectrochemistry. Both the iron centers and the *o*-dioxolene ligands of the complexes synthesized in this study were expected to exhibit redox activity. The family of tetranuclear complexes **4**, $\mathbf{5}^{-}$, and **6** was of particular interest in this regard, given the commonality in structural core, but variable number (**4** and $\mathbf{5}^{-}$) and differing redox state ($\mathbf{5}^{-}$ and **6**) of the *o*-dioxolene ligands. Although, **6** is derived from the one-electron chemical oxidation of $\mathbf{5}^{-}$, X-ray structural data (vide supra) indicate that a significant ligand rearrangement, involving the breaking and reforming of up to five Fe−O and Fe−N bonds, accompanies this oxidation. Thus, comparative voltammetric studies of $\mathbf{5}^{-}$ and **6** were expected to provide important insights into this structural rearrangement.

The voltammetric responses of $\mathbf{5}^{-}$ in dichloromethane solution containing either $[Bu_4N][B(C_6F_5)_4]$ or $[Bu_4N][PF_6]$ as the supporting electrolyte are similar for the first three oxidations as well as the reduction processes. However, electrode fouling that requires periodic cleaning of the electrode surface is encountered when the fourth oxidation process is involved in the potential scan with $[Bu_4N][PF_6]$ as the electrolyte. Thus unless otherwise specified, the voltammetric data presented here refer to the use of $[Bu_4N][B(C_6F_5)_4]$ as the supporting electrolyte. Cyclic and square wave voltammograms of complex $\mathbf{5}^{-}$ (Figure 5) reveal the presence of four well separated oxidation processes having formal potentials ($E^0_f(n)$, $n = 1-4$) of −0.27, 0.09, 0.52, and 0.89 V versus $[Cp_2Fe]^{0/+}$ (Table 7), in the potential range 0 to +1.50 V, consistent with the presence of four oxidizable 3,5-$DBCat^{2-}$ ligands. The E^0_f values were calculated from the average of oxidation (E_p^{ox}) and reduction (E_p^{red}) peak potentials $(E_p^{ox}+E_p^{red})/2$, assuming that the oxidized and reduced components have equal diffusion coefficients. Scanning the potential in the negative direction (0 to −2.50 V) led to the detection of a chemically reversible reduction process at ∼ −1.36 V attributable to one-electron metal-based Fe(III) to Fe(II) step, together with a chemically irreversible one at a very negative potential, $E_p^{red} = -2.02$ V.

Scheme 2. [28]

$$\mathbf{5}^{-} \underset{E^0_f(1)}{\overset{-e^-}{\rightleftharpoons}} \mathbf{5} \underset{E^0_f(2)}{\overset{-e^-}{\rightleftharpoons}} \mathbf{5}^{+} \underset{E^0_f(3)}{\overset{-e^-}{\rightleftharpoons}} \mathbf{5}^{2+} \underset{E^0_f(4)}{\overset{-e^-}{\rightleftharpoons}} \mathbf{5}^{3+} \quad \text{(ligand-based oxidation)}$$

$$\mathbf{5}^{-} \underset{E^0_f(-1)}{\overset{+e^-}{\rightleftharpoons}} \mathbf{5}^{2-} \quad \text{(metal-based reduction)}$$

The diffusion-controlled nature of the oxidation processes was confirmed under conditions of cyclic voltammetry by the linear plots of the peak currents, I_p^{ox}, versus the square root of scan rate ($\nu^{1/2}$), which passed through the origin. In addition, Anson plots (not shown) constructed from double potential step chronocoulometric measurements performed at step times of 0.5 to 10 s over the potential range relevant to each oxidation process established the absence of reactant or product adsorption. The peak-to-peak separations ($\Delta E_p = E_p^{ox} - E_p^{red}$) for the first three oxidation processes (76, 82, and 89 mV, respectively, at a scan rate of 100 mV s^{-1}) are similar to values obtained for the known electrochemically reversible one-electron oxidation of decamethylferrocene under the same conditions, thereby indicating that these

(26) Benelli, C.; Dei, A.; Gatteschi, D.; Pardi, L. *Inorg. Chem.* **1989**, *28*, 1476.

(27) Dei, A. *Inorg. Chem.* **1993**, *32*, 5730.

(28) No assumption relating to electronic distribution can be inferred from the given formulations.

Table 7. E^0_f Values[a] (volts versus $[Cp_2Fe]^{0/+}$) in CH_2Cl_2 Obtained by Cyclic Voltammetry with a 1.5 mm Diameter Glassy Carbon Electrode at a Scan Rate of 100 mV s^{-1}

		$Fe^{III/II}$ reduction	*o*-dioxolene reduction/oxidation			
complex	electrolyte	$E^0_f(-1)$	$E^0_f(1)$	$E^0_f(2)$	$E^0_f(3)$	$E^0_f(4)$
$\mathbf{5}^-$	$[Bu_4N][B(C_6F_5)_4]$	−1.36[b]	−0.27	0.09	0.52	0.89
$\mathbf{5}^-$	$[Bu_4N][PF_6]$	−1.33[b]	−0.25	0.11	0.51	0.75
6[c]	$[Bu_4N][B(C_6F_5)_4]$	−1.03	−0.59[d]	0.12[e]	0.57	0.86
6[c]	$[Bu_4N][PF_6]$	−1.02	−0.57[d]	0.13[e]	0.53	0.69
4[f]	$[Bu_4N][B(C_6F_5)_4]$	−0.80	−0.10	0.18		

[a] Calculated from $(E_p^{red} + E_p^{ox})/2$. [b] An irreversible reduction process also was detected with $E_p^{red} = -2.02$ V. [c] In the text the processes are labeled as P_a, P_b, P_c, P_d and P_e, respectively. [d] This process is a reduction. [e] This process is a two-electron oxidation. [f] Not studied with $[Bu_4N][PF_6]$ as the electrolyte because of poor solubility.

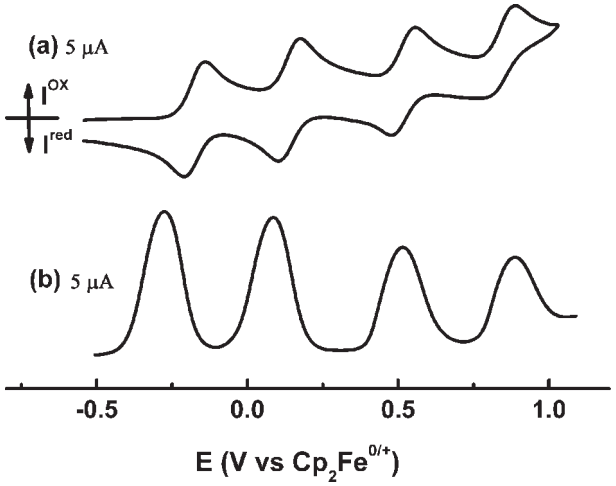

Figure 5. (a) Cyclic voltammogram of $\mathbf{5}^-$ (2.0 mM in CH_2Cl_2 with 0.05 M $[Bu_4N][B(C_6F_5)_4]$) obtained with a 1.5 mm diameter glassy carbon electrode at a scan rate of 100 mV s^{-1}. (b) Square wave voltammogram obtained under the same conditions with an amplitude of 25 mV and a frequency of 25 Hz.

electron transfer processes are fast (electrochemically reversible) and also monoelectronic. The small deviation from the value of 56 mV predicted theoretically for a reversible process is attributed to uncompensated resistance, R_u, and hence Ohmic IR_u drop. The ΔE_p value for the fourth oxidation process ($\Delta E_p = 115$ mV) is slightly larger than expected for an ideal reversible one-electron oxidation process, even after allowance for IR_u drop. Non ideality is also evident in the square-wave voltammogram (Figure 5b) where the magnitude of the peak current for the fourth process is smaller than for the preceding ones. Chemical reversibility was readily established for the first three oxidation processes, with $|I_p^{ox}/I_p^{red}|$ values being close to unity, indicating that the products of oxidation are persistent on the cyclic voltammetric time scale, even when using a scan rate of 100 mV s^{-1}. However, fast scan rates ($\nu \geq 1.0$ V s^{-1}) are required to improve the reversibility of the fourth oxidation process. On the basis of these data, it is probable that each electron-transfer step associated with oxidation of $\mathbf{5}^-$ (Scheme 2) involves fast and reversible oxidation of one of the coordinated 3,5-$DBCat^{2-}$ ligands to the corresponding 3,5-$DBSQ^-$, without change in the binding modes and positions of the ligands. However, some rearrangement may be associated with the fourth oxidation process. The net result of the oxidative voltammetric behavior is that the overall charge on the tetranuclear complex, $\mathbf{5}^-$, increases from −1 to +3 (Scheme 2).

The differences in the E^0_f values (Table 7) derived for the four successive one-electron oxidation processes associated with monoanionic $\mathbf{5}^-$, expressed as $\Delta E_1 = E^0_f(2) - E^0_f(1)$, $\Delta E_2 = E^0_f(3) - E^0_f(2)$, and $\Delta E_3 = E^0_f(4) - E^0_f(3)$ are 0.36, 0.43, and 0.37 V, respectively. The total separation between the first and fourth oxidation processes is 1.16 V. The comproportionation constants, K_{comp}, calculated from these ΔE values and eq 8

$$\log K_{comp} = 16.9 \times \Delta E \quad \text{at} \quad 298\ \text{K} \qquad (\Delta E \text{ in V}) \tag{8}$$

are 1.21×10^6, 1.85×10^7, and 1.79×10^6, respectively. The similarity of the individual ΔE values and the agreement with those reported for structurally related polynuclear osmium−dioxolene complexes supports the hypothesis that these oxidation processes are all ligand-based and involve a similar level of electronic interaction.[29]

Confirmation that one electron is transferred during each oxidation process and an assessment of the stability of the first one-electron oxidation product, neutral **5**, over longer time scales was achieved by controlled potential bulk electrolysis experiments using a Pt-gauze working electrode. Exhaustive oxidative bulk electrolysis of $\mathbf{5}^-$ at $E_{appl} = -0.1$ V in dichloromethane with 0.1 M $[Bu_4N][PF_6]$ at 295 K led to a slight change in the intensity of the deep blue color of the solution. Coulometric analysis of the data indicated that under these conditions $n = 1.00 \pm 0.05$, with the deep blue color of the solution of the generated one-electron oxidized product persisting for at least 30 min. Voltammetry (Figure 6) performed at steady state conditions ($\nu = 2.0$ mV s^{-1}) before and immediately after bulk electrolysis indicate that the starting material had converted quantitatively to the oxidized product, as the same half wave potential and voltammetric profiles were observed, differing only in the sign of the current. Reductive back electrolysis at $E_{appl} = -0.5$ V regenerated $\mathbf{5}^-$ in 90 ± 5% yield. UV−visible spectral monitoring of the one-electron oxidized material was performed ex situ by syringe removal of samples before and after bulk electrolysis or in situ by Optically Transparent Thin-Layer Electrolysis (OTTLE) experiments, conducted at $E_{appl} = -0.1$ V at a platinum gauze electrode (Figure 6b). In both cases, the weak and broad bands of $\mathbf{5}^-$ at 425 and 610 nm (Table 6) decreased in intensity during the course of electrolysis, with the oxidized material exhibiting four broad bands at 388, 430,

(29) Barthram, A. M.; Reeves, Z. R.; Jeffery, J. C.; Ward, M. D. *J. Chem. Soc., Dalton Trans.* **2000**, 3162.

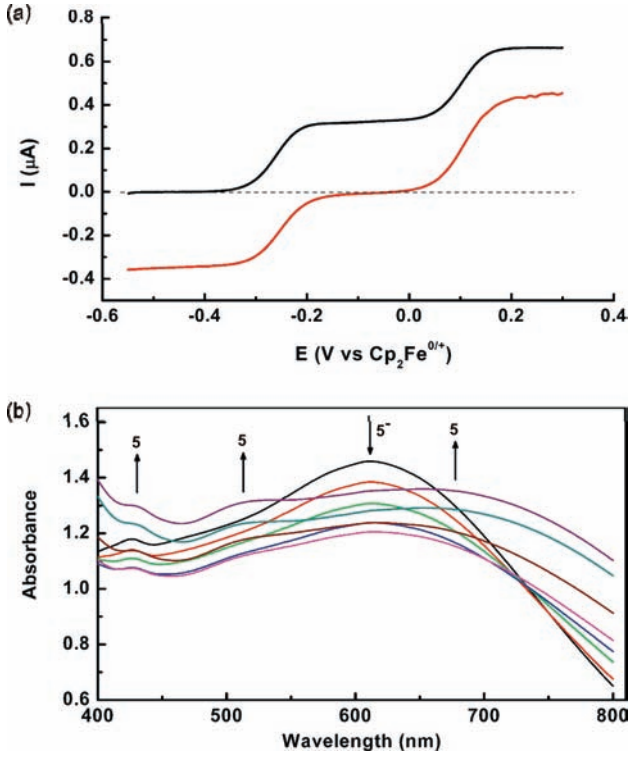

Figure 6. (a) Linear sweep voltammograms of $\mathbf{5}^-$ (0.7 mM in CH_2Cl_2 with 0.1 M $[Bu_4N][PF_6]$) obtained with a 1.0 mm diameter glassy carbon electrode at a scan rate of 2.0 mV s^{-1} before (black curve) and after (red curve) one-electron bulk electrolysis at $E_{appl} = -0.1$ V. (b) Spectroelectrochemical monitoring of the changes in the visible spectrum during the course of the electrolysis.

512, and 660 nm. An isosbestic point was observed at 727 nm during the initial stages of electrolysis, but not at longer times, indicative of a slow structural rearrangement or another form of instability of neutral **5**.

Neutral compound **6**, which was obtained from the one-electron chemical oxidation of complex $\mathbf{5}^-$, exhibits significantly different voltammetric behavior to that found with the parent complex $\mathbf{5}^-$ and its one-electron electrochemically oxidized product **5**, in terms of formal reversible potentials and other features. This is attributed to retention of the molecular structure of **5** following oxidation of $\mathbf{5}^-$ on the cyclic voltammetry time scale, which is in contrast to the significant structural rearrangement that accompanies the longer time scale chemical oxidation of $\mathbf{5}^-$ to **6**. Thus, **6** displays five reversible processes (Figure 7), consisting of three oxidations (P_c, P_d, and P_e) with E^0_f values of 0.12, 0.57, and 0.86 V, respectively, and two reductions (P_a and P_b) with $E^0_f = -0.59$ and -1.03 V (Table 7). The assignment of oxidation or reduction was achieved from the sign of the current (positive = oxidation, negative = reduction) of steady-state voltammograms obtained with a rotating disk electrode (not shown). Detailed analysis of the voltammetric data reveals that the magnitude of the current associated with the first oxidation step (P_c) is close to double that of both the second oxidation (P_d) and the first reduction process (P_a), which in turn have similar current per unit concentration values to that of the one-electron oxidation of $\mathbf{5}^-$, for experiments undertaken under the same conditions. Thus, process P_c is assigned as a two-electron rather than one-electron oxidation

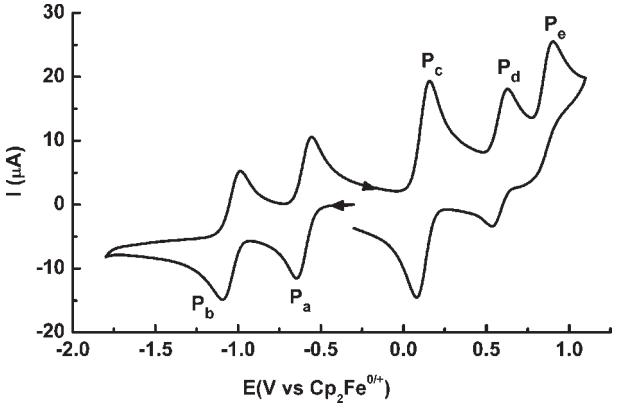

Figure 7. Cyclic voltammogram of **6** (1.2 mM in CH_2Cl_2 with 0.05 M $[Bu_4N][B(C_6F_5)_4]$) obtained with a 1.5 mm diameter glassy carbon electrode at a scan rate of 100 mV s^{-1}.

Scheme 3. [28]

$$\mathbf{6} \underset{P_c}{\overset{-2e^-}{\rightleftharpoons}} \mathbf{6}^{2+} \underset{P_d}{\overset{-e^-}{\rightleftharpoons}} \mathbf{6}^{3+} \underset{P_e}{\overset{-e^-}{\rightleftharpoons}} \mathbf{6}^{4+} \quad \text{(ligand-based oxidation)}$$

$$\mathbf{6} \underset{P_a}{\overset{+e^-}{\rightleftharpoons}} \mathbf{6}^{-} \underset{P_b}{\overset{+e^-}{\rightleftharpoons}} \mathbf{6}^{2-} \quad \text{(ligand- and metal-based reduction)}$$

process. This postulate was quantitatively confirmed by sequential controlled potential bulk electrolysis at $E_{appl} = -0.75$, 0.3, and 0.75 V, respectively, which showed that the oxidation process P_c involves the transfer of two electrons whereas processes P_a and P_d are associated with single one-electron transfer steps.

Although the E^0_f values for the three oxidation processes [P_c ($n = 2$), P_d ($n = 1$), and P_e ($n = 1$)] of **6** closely match their counterparts ($n = 1$) in $\mathbf{5}^-$, the E^0_f value of the first one-electron reduction process (P_a) is dramatically shifted by about 0.32 V to more negative potential compared to the first one-electron oxidation process in $\mathbf{5}^-$ (i.e., -0.59 for **6** compared to -0.27 V for $\mathbf{5}^-$). On the basis of the E^0_f values of the parent complex $\mathbf{5}^-$, the single two-electron oxidation process (P_c) can be assigned to the simultaneous oxidation of the 3,5-$DBSQ^-$ ligand and one of the three 3,5-$DBCat^{2-}$ ligands to a 3,5-DBQ ligand and another 3,5-$DBSQ^-$ ligand, respectively (Scheme 3). Therefore, the two most positive oxidation processes (P_d and P_e) are assigned to the oxidation of the remaining two 3,5-$DBCat^{2-}$ ligands to the 3,5-$DBSQ^-$ forms. On the reduction side, the first process (P_a) is attributed to the one-electron reduction of neutral **6** to an anionic species $\mathbf{6}^-$. Cyclic and linear sweep voltammetry ($\nu = 1-2$ mV s^{-1}) recorded after one-electron reductive bulk electrolysis of **6** provides no evidence for reconversion of the coordinated 3,5-$DBSQ^-$ ligand in **6** back to the 3,5-$DBCat^{2-}$ form in $\mathbf{6}^-$. This finding suggests that this ligand-based reduction process does not involve change in the coordination modes and/or the structure at least on this experimental time scale. Since there is no further ligand-based reduction possible at the reversible potential of the second reduction process (P_b), we assign this process to the metal-based Fe(III) to Fe(II) reduction.

The striking differences in the electrochemical properties of the chemically and electrochemically generated one-electron oxidation products of $\mathbf{5}^-$, that is, **5** and **6**, suggest that the two methods of oxidation produce

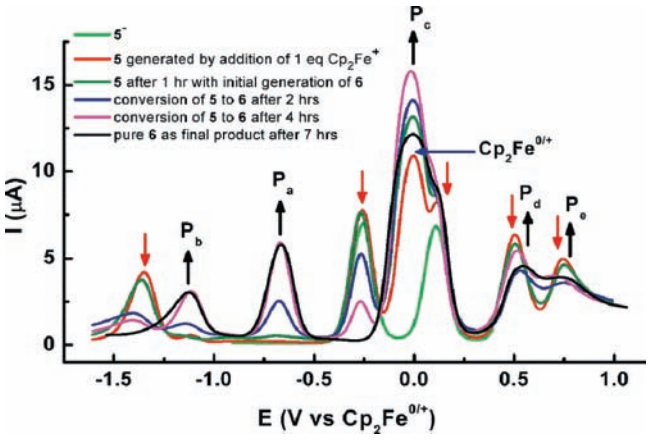

Figure 8. Square wave voltammograms recorded during the chemical oxidation of $\mathbf{5}^-$ (0.0037 mmol in CH_2Cl_2 with 0.1 M $[Bu_4N][PF_6]$) with 1.0 equiv of $[Cp_2Fe][PF_6]$ over a period of 7 h, obtained with a 1.5 mm diameter glassy carbon electrode at a frequency of 15 Hz.

structurally different compounds. To confirm this hypothesis, chemical oxidation of $\mathbf{5}^-$ (0.0037 mmol) with 1.0 equiv of $[Cp_2Fe][PF_6]$ was undertaken in an electrochemical cell containing 1.5 mL of dichloromethane with 0.1 M $[Bu_4N][PF_6]$ as the electrolyte. The progress of the reaction was monitored voltammetrically, which revealed the initial generation of the same one-electron oxidation product, **5**, obtained via bulk electrolysis (identical E^0_f values and voltammetric characteristics). However, voltammetric monitoring over a period of 7 h, which mimics the time scale associated with synthesis and crystallization of the chemically oxidized product **6**, led to detection of the voltammetric features associated with **6**. Thus as shown in Figure 8, the processes with E^0_f values of −1.30 and −0.25 V in $\mathbf{5}^-$ are fully replaced by processes with E^0_f values of −1.0 and −0.57 V (similar to processes P_b and P_a, respectively, for **6**) whereas the process at $E^0_f = 0.11$ V shifts to more negative potential and grows with time to a new process (P_c) that overlays that for ferrocene. The two most positive oxidation processes seen initially in $\mathbf{5}^-$ are slightly changed with time upon oxidation with $[Cp_2Fe][PF_6]$, but after 7 h their potentials match those of processes P_d and P_e in **6**. These results clearly indicate that chemical and electrochemical oxidation of $\mathbf{5}^-$ by one-electron initially produce the same product, **5**, which upon prolonged periods of time undergoes a major structural rearrangement to yield **6** as the final product. This conclusion, reached on the basis of voltammetry, is supported by the identical nature of the UV−visible spectra obtained for **6** and for the electrochemically generated one-electron oxidized species, **5**, when left for an extended period of time. The combined electrochemical and spectroscopic results from the solution studies are consistent with the significant structural differences between $\mathbf{5}^-$ and **6** in the solid state, as determined by X-ray crystallography. The redox-initiated structural rearrangement involves breaking and reforming five Fe−O and Fe−N bonds to alter the binding positions and modes (Figure 2) of one of the coordinated Schiff-base L^{2-} ligands (from a μ_3-mode in $\mathbf{5}^-$ and presumably **5**, to a μ_4-mode in **6**) and one of the *o*-dioxolene ligands (from a μ_2-bridging 3,5-$DBCat^{2-}$ in $\mathbf{5}^-$ and presumably **5**, to a chelating-only 3,5-$DBSQ^-$ ligand in **6**). Complexes **5** and **6** are structural isomers, with **5** the kinetic product of one-electron oxidation of $\mathbf{5}^-$, while **6** is the thermodynamic product.

Scheme 4. [28]

$$\mathbf{4} \underset{E^0_f(1)}{\overset{-e^-}{\rightleftharpoons}} \mathbf{4}^+ \underset{E^0_f(2)}{\overset{-e^-}{\rightleftharpoons}} \mathbf{4}^{2+} \qquad \text{(ligand-based oxidation)}$$

$$\mathbf{4} \underset{E^0_f(-1)}{\overset{+e^-}{\rightleftharpoons}} \mathbf{4}^- \qquad \text{(metal-based reduction)}$$

Voltammetry of a solution of complex **4** reveals two well-defined oxidation processes (Supporting Information, Figure S2), as expected from the presence of two oxidizable 3,5-$DBCat^{2-}$ ligands (Scheme 4). On sweeping the potential in the reverse direction, a new reduction process is seen at $E_p^{red} = -0.40$ V. This peak is not observed upon switching the potential immediately after the first oxidation process (0.1 V), indicating that it is associated with the second oxidation process. The chemical reversibility of the second oxidation process dramatically improves as the scan rate is increased (black curve in Supporting Information, Figure S2), suggesting that the electron-transfer step for the second process is accompanied by a moderately fast follow-up chemical reaction. This reaction may involve structural rearrangement of the coordinated 3,5-$DBCat^{2-}$ ligands from a μ_2-bridging mode to a chelating mode following the one-electron oxidation and conversion to the 3,5-$DBSQ^-$ ligands, as is observed in the formation of **6** following one-electron oxidation of $\mathbf{5}^-$. The apparently enhanced rate of structural rearrangement of **4** versus $\mathbf{5}^-$ may be associated with the presence of only two 3,5-$DBCat^{2-}$ ligands in **4** compared to four in $\mathbf{5}^-$, which, in the latter, would be more efficient in stabilizing the isostructural oxidized species.

The structural difference between **4** and $\mathbf{5}^-$ is also evident from the marked difference in their reversible potentials. Thus, the E^0_f values of the two oxidation processes of **4**, measured at a scan rate of 100 mV s^{-1} ($E^0_f(1) = -0.10$, $E^0_f(2) = 0.18$ V) differ by +0.170 and +0.090 V, respectively, to more positive values relative to the first two oxidation processes of $\mathbf{5}^-$ (Table 1). Similarly, the metal-based Fe(III) to Fe(II) reduction occurs at $E^0_f = -0.80$ V, which is significantly more positive than the value of −1.36 V obtained for the Fe(III) to Fe(II) reduction of $\mathbf{5}^-$. The electronic effect that arises from effectively replacing two 3,5-$DBCat^{2-}$ ligands in $\mathbf{5}^-$ with two extra phenolate Schiff base ligands (L^{2-}) in **4** has a similar effect on the E^0_f as is the case when an electron withdrawing substituent is removed from the catechol ring. This can be understood given that the oxidation will be thermodynamically more facile when electron density flows into the catechol ring, thereby leading to stabilization of the positively charged cationic species generated during the oxidation processes. Thus, the overall thermodynamic stabilization of the oxidized products of **4**, expressed as $\Delta E = 0.28$ V and $K_{comp} = 5.4 \times 10^4$ (determined using eq 8), is significantly lower than that for $\mathbf{5}^-$.

Magnetochemistry. Variable temperature magnetic susceptibility data collected at 0.1 T are plotted in Figures 9−11 and Supporting Information, Figure S8 for compounds **3**, **4**, **5a**, **6**, **7**, and **8a**, respectively, together with the fits of the

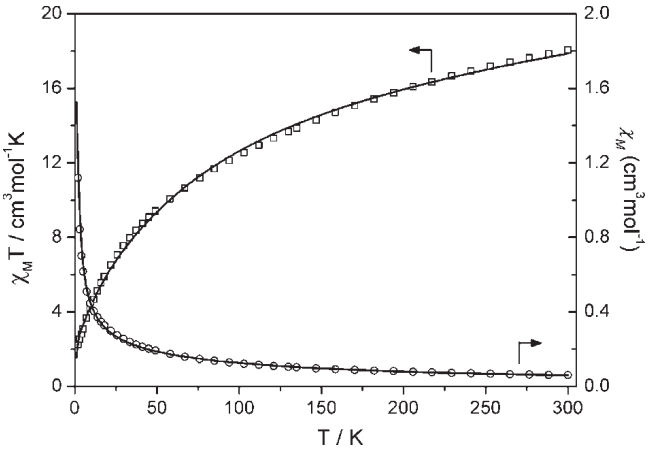

Figure 9. Plot of $\chi_M T$ and χ_M vs T for **3**. The solid lines are fits as described in the text.

Scheme 5

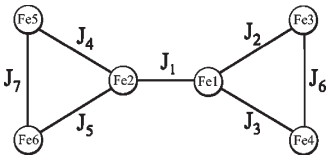

experimental data for **3**, **4**, **5a**, **7**, and **8a** and a simulation of the experimental data for **6**. Variable temperature magnetization data in the temperature range 2−5.5 K with magnetic fields up to 5 T are plotted in the Supporting Information, Figures S3−S7 and S9.

For **3** (Figure 9), $\chi_M T$ decreases gradually from 18.1 cm^3 mol^{-1} K at 300 K to 2.2 cm^3 mol^{-1} K at 2.0 K. The room temperature value is considerably lower than the spin only value of 26.3 cm^3 mol^{-1} K calculated for six non-interacting high spin Fe(III) centers with $g = 2.0$. This behavior is consistent with competing antiferromagnetic interactions of considerable magnitude. The coupling scheme appropriate to the magnetic core of **3** is presented in Scheme 5, with the low symmetry of the complex requiring seven different coupling constants.

This coupling scheme gives rise to the exchange Hamiltonian:

$$\hat{H}_{ex} = -2J_1(\boldsymbol{S}_1\cdot\boldsymbol{S}_2) - 2J_2(\boldsymbol{S}_1\cdot\boldsymbol{S}_3) - 2J_3(\boldsymbol{S}_1\cdot\boldsymbol{S}_4) - 2J_4(\boldsymbol{S}_2\cdot\boldsymbol{S}_5) - 2J_5(\boldsymbol{S}_2\cdot\boldsymbol{S}_6) - 2J_6(\boldsymbol{S}_3\cdot\boldsymbol{S}_4) - 2J_7(\boldsymbol{S}_5\cdot\boldsymbol{S}_6) \quad (9)$$

To fit the magnetic susceptibility data to the theoretical expression, simplifications of the model were necessary to avoid the overparametrization of the fit. No satisfactory fit of the data could be obtained with a one J model ($J_1 = J_2 = J_3 = J_4 = J_5 = J_6 = J_7$) or two J models incorporating the pseudo inversion center of **3** (e.g., J_1, $J_2 = J_3 = J_4 = J_5 = J_6 = J_7$). However, a model using three J values $J_1 = -26.9$ cm^{-1}, $J_3 = J_4 = -6.3$ cm^{-1} and $J_2 = J_5 = J_6 = J_7 = -3.0$ cm^{-1} with g fixed to 2.0 reproduced the experimental data very well (Figure 9). Small deviations from the experimental data were observed only at the lowest temperatures. The J values obtained give rise to an $S = 0$ ground state with multiple $S = 0$, $S = 1$, $S = 2$, and $S = 3$ excited states less than 10 cm^{-1} higher in energy.

Scheme 6

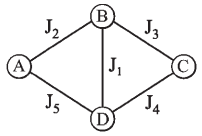

4: A = Fe1, B = Fe2, C = Fe1', D = Fe2'
5a: A = Fe1, B = Fe3, C = Fe4, D = Fe2

The magnetization isotherms at 2.0 and 3.0 K approach saturation at 1 T (Supporting Information, Figure S3), before rising steeply without saturation up to 5 T. This curve shape is indicative of a poorly isolated ground state with various close lying states of higher spin, a situation arising from the multiple pairwise antiferromagnetic interactions in the given spin topology. The failure to reproduce both $\chi_M T$ at the lowest measured temperatures and the isothermal magnetization curves above 0.5 T with simulations calculated using the parameters obtained from fitting the susceptibility data results from the overly simplified model employed to obtain this fit. Data at lower temperatures and an extended model with additional exchange parameters would be necessary to determine the complex energy level scheme for **3**.

For **4** (Figure 10a), $\chi_M T$ decreases steadily from a value of 10.1 cm^3 mol^{-1} K at 300 K to 0.1 cm^3 mol^{-1} K at 2.0 K. The room temperature value is substantially less than the calculated spin-only value of 17.5 cm^3 mol^{-1} K for four non-interacting Fe(III) centers with $g = 2.0$ and the behavior suggests overall antiferromagnetic interactions and an $S = 0$ ground state. Over the same temperature range, χ_M increases gradually before reaching a broad maximum at about 120 K and decreasing gradually as the temperature is decreased to 5 K. Below 5 K, χ_M increases rapidly as the temperature is decreased, which is attributed to the presence of a mononuclear Fe(III) paramagnetic impurity. The coupling scheme appropriate to a tetranuclear complex with a planar rhombic core, such as **4,** is depicted in Scheme 6.

The symmetry of the structure of **4** affords $J_2 = J_4$ and $J_3 = J_5$, while the similarity in the Fe1···Fe2 and Fe1···Fe2′ pathways (Table 3) suggests that $J_2 = J_3 = J_4 = J_5$ is a reasonable approximation. Thus the data between 2.0 and 300 K were fit to the exchange Hamiltonian:

$$\hat{H}_{ex} = -2J_1(\boldsymbol{S}_B\cdot\boldsymbol{S}_D) - 2J_2(\boldsymbol{S}_A\cdot\boldsymbol{S}_B + \boldsymbol{S}_B\cdot\boldsymbol{S}_C + \boldsymbol{S}_C\cdot\boldsymbol{S}_D + \boldsymbol{S}_A\cdot\boldsymbol{S}_D) \quad (10)$$

with g fixed to 2.0 and the inclusion of a term to account for a monomeric Fe(III) impurity. Efforts to fit the data with $J_1 = J_2$ did not yield a good fit and the best fit for $J_1 \neq J_2$ was obtained with $J_1 = 0$ cm^{-1}, $J_2 = -9.3$ cm^{-1} and 0.6% monomeric Fe(III) $S = 5/2$ paramagnetic impurity (solid lines in Figure 10a). This gives rise to a well-isolated $S = 0$ ground state with an $S = 1$ first excited state 19 cm^{-1} above the ground state. Low temperature magnetization measurements (Supporting Information, Figure S4) are also consistent with a well-isolated $S = 0$ ground state and a small amount of paramagnetic impurity.

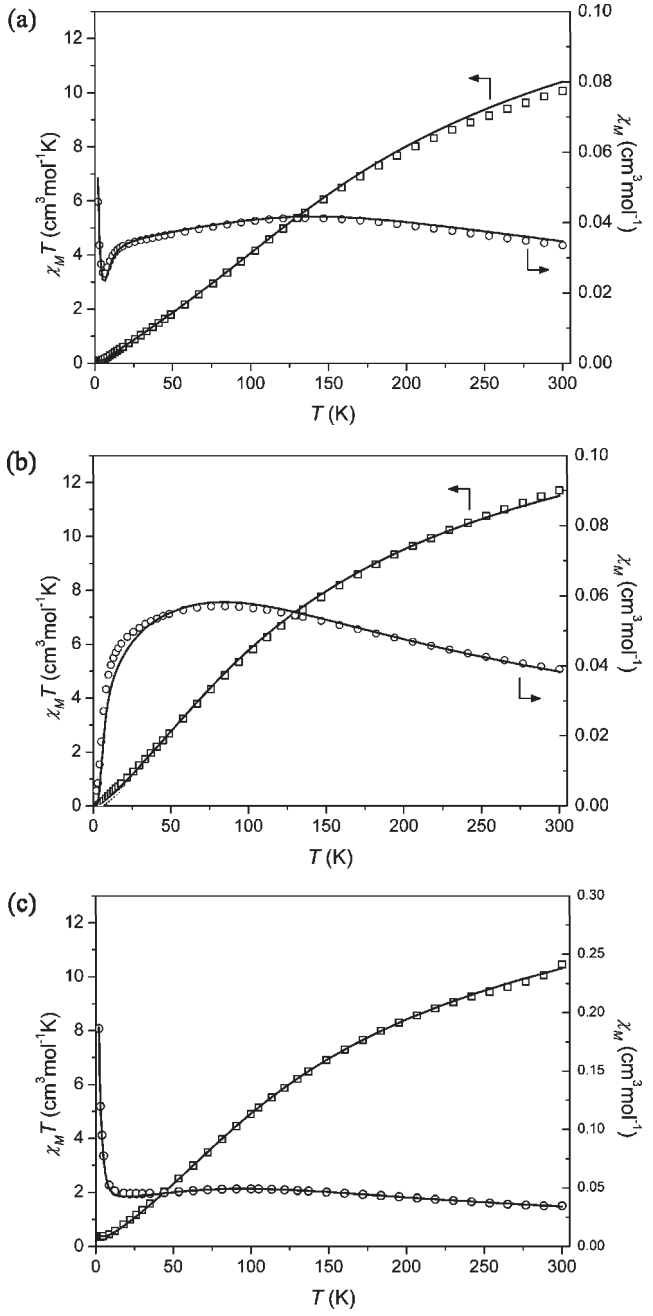

Figure 10. Plot of $\chi_M T$ and χ_M vs T for (a) **4**, (b) **5a**, and (c) **6**. The solid lines are fits or simulations as described in the text.

The thermal variation of the magnetic susceptibility of compound **5a** (Figure 10b) is similar to that observed for **4** (Figure 10a). For **5a**, $\chi_M T$ decreases steadily from a value of 11.7 cm^3 mol^{-1} K at 300 K to 0.01 cm^3 mol^{-1} K at 2.0 K. The maximum in χ_M occurs at 85 K, and there is no low temperature increase, indicating no paramagnetic impurity. The behavior is again consistent with overall antiferromagnetic interactions and an $S = 0$ ground state for complex $\mathbf{5}^-$. The lack of symmetry in $\mathbf{5}^-$ does not allow the approximations made in the fitting of the data for **4**; however for simplicity, initial attempts to fit the data between 2.0 and 300 K commenced with the two J model described by the exchange Hamiltonian (eq 10). With g again fixed to 2.0, efforts to fit the data with $J_1 = J_2$ did not give a good fit to the experimental data. However, a good

Scheme 7

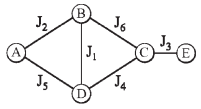

6: A = Fe3, B = Fe1, C = Fe2, D = Fe4, E = 3,5-DBSQ$^-$

fit was obtained with $J_1 = -3.5$ cm^{-1} and $J_2 = -7.0$ cm^{-1} (Figure 10b). The adequacy of this fit attests to the validity of the approximations made and the incorporation of additional J values was not pursued to avoid overparameterizing the solution. The fitting parameters obtained again give rise to an $S = 0$ ground state, this time with an $S = 1$ first excited state 14 cm^{-1} above the ground state. Low temperature magnetization measurements (Supporting Information, Figure S5) are also consistent with a well-isolated $S = 0$ ground state and no paramagnetic impurity.

For **6** (Figure 10c), the value of $\chi_M T$ at 300 K is 10.5 cm^3 mol^{-1} K, which is considerably lower than the value of 17.9 cm^3 mol^{-1} K calculated four non-interacting high spin Fe(III) ($S = 5/2$) centers with a 3,5-DBSQ$^-$ radical ($S = 1/2$) ligand, suggesting significant antiferromagnetic interactions. As the temperature is decreased the value of $\chi_M T$ decreases steadily to reach 0.37 cm^3 mol^{-1} K at 2.0 K, which suggests an $S = 1/2$ ground state for the complex. Over the same temperature range, χ_M increases gradually to reach a broad maximum at 90 K before decreasing and then rapidly increasing below 10 K. The coupling scheme appropriate to complex **6** is depicted in Scheme 7.

This scheme is derived from that applied to the structurally related complexes **4** and $\mathbf{5}^-$, although it is extended to include the radical 3,5-DBSQ$^-$ ligand. This ligand chelates Fe2 (vide supra) and does not bridge to any of the other Fe centers; thus, the possibility of magnetic coupling between the radical ligand and the other Fe centers has been discounted. Again the similarity in the Fe1···Fe2, Fe1···Fe3, Fe2···Fe4, and Fe3···Fe4 pathways (Table 3) suggests that $J_2 = J_4 = J_5 = J_6$ is a reasonable approximation. Thus the exchange Hamiltonian

$$\hat{H}_{ex} = -2J_1(\boldsymbol{S}_B \cdot \boldsymbol{S}_D) - 2J_2(\boldsymbol{S}_A \cdot \boldsymbol{S}_B + \boldsymbol{S}_B \cdot \boldsymbol{S}_C + \boldsymbol{S}_C \cdot \boldsymbol{S}_D + \boldsymbol{S}_A \cdot \boldsymbol{S}_D) - 2J_3(\boldsymbol{S}_C \cdot \boldsymbol{S}_E) \quad (11)$$

was employed to simulate the experimental susceptibility data. For this simulation g was fixed to 2.0, which is appropriate for both high spin Fe(III) $S = 5/2$ centers and the organic 3,5-DBSQ$^-$ ($S = 1/2$) radical. The coupling constant between Fe2 and the radical ligand, J_3, was fixed to -600 cm^{-1}, while J_1 and J_2 were varied systematically. This value of -600 cm^{-1} for J_3 was obtained from the least-squares fit of the magnetic susceptibility data for the structurally related complex [Fe(salen)(3,5-DBSQ)], in which a 3,5-DBSQ$^-$ ligand chelates an Fe(III) center in a similar manner to that observed in **6**.[30] Extremely strong antiferromagnetic coupling has been observed in this and other high spin Fe(III) complexes of 3,5-DBSQ$^-$.[31]

(30) Kessel, S. L.; Emberson, R. M.; Debrunner, P. G.; Hendrickson, D. N. *Inorg. Chem.* **1980**, *19*, 1170.

(31) (a) Buchanan, R. M.; Kessel, S. L.; Downs, H. H.; Pierpont, C. G.; Hendrickson, D. N. *J. Am. Chem. Soc.* **1978**, *100*, 7894. (b) Cohn, M. J.; Xie, C. L.; Tuchagues, J. P. M.; Pierpont, C. G.; Hendrickson, D. N. *Inorg. Chem.* **1992**, *31*, 5028.

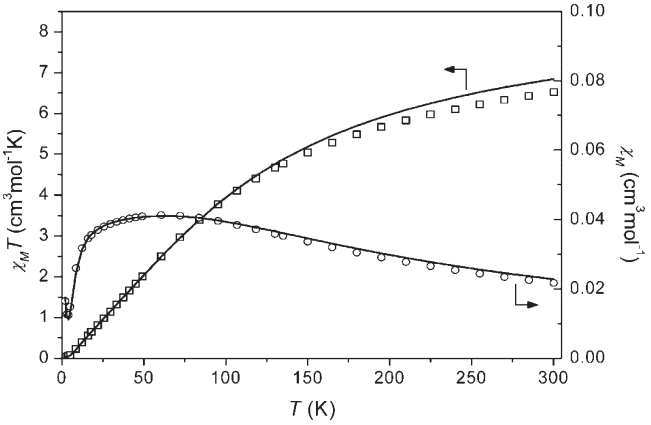

Figure 11. Plot of $\chi_M T$ and χ_M vs T for **7**. The solid lines are fits as described in the text.

An excellent reproduction of the χ_M and $\chi_M T$ versus T data was obtained with $J_1 = -4.0$ cm^{-1}, $J_2 = -7.5$ cm^{-1}, $J_3 = -600$ cm^{-1}, and $g = 2.0$ (solid line in Figure 10c). It is noteworthy that the values of J_1 and J_2 are very close to the equivalent coupling constants obtained for complex $\mathbf{5}^-$, which has a very similar magnetic core. These parameters give rise to an $S = 1/2$ ground state for complex **6** with an $S = 3/2$ first excited state that is 24 cm^{-1} above the ground state. Variable temperature magnetization data between 2 and 5.5 K are plotted in Supporting Information, Figure S6. The isotherms for 2.0, 3.0, 4.0, and 5.5 K are essentially superimposable, and the magnetization value of 1.0 Nβ at 2.0 K and 5.0 T is consistent with an $S = 1/2$ ground state with $g = 2.0$. However, a slight deviation at large values of H/T from the Brillouin function calculated for an $S = 1/2$ system with $g = 2.0$ may indicate the presence of $S > 1/2$ excited states lying at lower energy than the $S = 3/2$ first excited state calculated using the J values derived from the susceptibility fit.

For **7** (Figure 11), $\chi_M T$ decreases steadily from a value of 6.5 cm^3 mol^{-1} K at 300 K to 0.03 cm^3 mol^{-1} K at 2.0 K. The room temperature value is less than the calculated spin-only value of 8.8 cm^3 mol^{-1} K for two non-interacting Fe(III) centers with $g = 2.0$, and the behavior is consistent with antiferromagnetic coupling between the two Fe centers and an $S = 0$ ground state. Over the same temperature range, χ_M increases gradually before reaching a broad maximum at about 60 K and decreasing gradually as the temperature is decreased to 4 K. Below 4 K, χ_M increases rapidly as the temperature is decreased, suggesting the presence of a paramagnetic impurity. The data between 2.0 and 300 K were fit to the exchange Hamiltonian:

$$\hat{H}_{ex} = -2J(\boldsymbol{S}_1 \cdot \boldsymbol{S}_2) \qquad (12)$$

with g fixed to 2.0 and the inclusion of a term to account for a monomeric Fe(III) impurity. The best fit was obtained with $J_1 = -8.0$ cm^{-1} and 0.4% paramagnetic impurity (solid lines in Figure 11). This gives rise to a well-isolated $S = 0$ ground state with an $S = 1$ first excited state 16 cm^{-1} above the ground state. Low temperature magnetization measurements (Supporting Information, Figure S7) are consistent with a well-isolated $S = 0$ ground state and a small amount of paramagnetic impurity.

The thermal variation of the magnetic susceptibility of **8a** (Supporting Information, Figure S7) is very similar to that observed for **7**. For **8a**, $\chi_M T$ again decreases steadily from a value of 6.5 cm^3 mol^{-1} K at 300 K to 0.03 cm^3 mol^{-1} K at 2.0 K. The maximum in χ_M occurs at 70 K, and the low temperature increase again suggests a small amount of paramagnetic impurity. The data between 2.0 and 300 K were fit to the exchange Hamiltonian (eq 12) with g fixed to 2.0 and the inclusion of a term to account for a monomeric Fe(III) impurity. The best fit was obtained with $J_1 = -8.5$ cm^{-1} and 0.3% paramagnetic impurity (solid lines in Supporting Information, Figure S8). This gives rise to a well-isolated $S = 0$ ground state with an $S = 1$ first excited state 17 cm^{-1} above the ground state. Low temperature magnetization measurements (Supporting Information, Figure S9) are again consistent with a well-isolated $S = 0$ ground state and a small amount of paramagnetic impurity.

The single crystal X-ray structures for solvated compounds **3**, **5a**, **6**, **7**, and **8a** were determined at 130 K, while the structural data for solvated compound **4** were collected at 295 K. In every case all Fe−O and Fe−N bond lengths, and the resulting bond valence sum calculations, are consistent with Fe(III) centers at these temperature (vide supra). The magnetic susceptibility data for these compounds were measured between 2 and 300 K, and the data are consistent with high spin Fe(III) centers across this temperature range. There is no evidence for any low spin Fe(III) contribution, which would be unusual for the ligand fields associated with the $\{O_6\}$ or $\{O_5N\}$ donor sets that are present in the present complexes. In addition, there is no magnetic evidence for the presence of any Fe(II) centers, nor any indication of any thermally induced valence tautomeric transitions from Fe(III)-catecholate at low temperature to Fe(II)-semiquinone at high temperature.

Magnetostructural Correlations. A useful magnetostructral correlation has been developed recently by Christou et al. for polynuclear ferric complexes with oxo, hydroxo, and alkoxo bridges.[32] This was in part derived from earlier models for dinuclear ferric complexes proposed by Gorun and Lippard and subsequently Weihe and Güdel.[33] The Christou model encompasses both the radial and angular dependence of the exchange constant, such that the interaction becomes more strongly antiferromagnetic as the Fe−O distance and the Fe−O−Fe angle increase. The angular dependence is accentuated as the Fe−O distance decreases and the radial dependence is more important at larger Fe−O−Fe angles.

Table 8 presents the coupling constants determined from fitting or simulating the magnetic susceptibility data for compounds **3**, **4**, **5a**, **6**, **7**, and **8a**, together with the values calculated using the Christou model. These calculated values employ the Fe−O distances and Fe−O−Fe angles derived from the crystallographic data. In general there is very good agreement between the experimentally derived and calculated values, bearing in mind that simplified coupling schemes were employed for the present

(32) Canada-Vilalta, C.; O'Brien, T. A.; Brechin, E. K.; Pink, M.; Davidson, E. R.; Christou, G. *Inorg. Chem.* **2004**, *43*, 5505.
(33) (a) Gorun, S. M.; Lippard, S. J. *Inorg. Chem.* **1991**, *30*, 1625. (b) Weihe, H.; Güdel, H. U. *J. Am. Chem. Soc.* **1997**, *119*, 6539.

Table 8. Fe···Fe Exchange Interactions for Compounds **3**, **4**, **5a**, **6**, **7**, and **8a**

		J (cm^{-1})	
compound	linkage	from fit or simulation of susceptibility data	calculated[a]
3	$(\mu_2\text{-OR})_2$	−26.9	−9.2
	$(\mu_2\text{-OR})(\mu_3\text{-OR})$	−3.0, −6.3	−7.2, −7.6, −9.3, −10.1
	$(\mu_2\text{-OR})(\mu_3\text{-OR})(\mu_2\text{-OAc})$	−3.0	−8.4, −10.5
4	$(\mu_3\text{-OR})_2$	0	−2.8
	$(\mu_2\text{-OR})(\mu_3\text{-OR})$	−9.3	−9.1, −11.2
5a	$(\mu_3\text{-OR})_2$	−3.5	−3.9
	$(\mu_2\text{-OR})(\mu_3\text{-OR})$ or $(\mu_2\text{-OR})(\mu_3\text{-OR})(\mu_2\text{-OAc})$	−7.0	−6.4, −7.5, −8.6, −11.6
6	$(\mu_3\text{-OR})_2$	−4.0	−3.6
	$(\mu_2\text{-OR})(\mu_3\text{-OR})$ or $(\mu_2\text{-OR})(\mu_3\text{-OR})(\mu_2\text{-OAc})$	−7.5	−6.4, −7.1, −10.7, −11.5
7	$(\mu_2\text{-OR})_2$	−8.0	−9.8
8a	$(\mu_2\text{-OR})_2$	−8.5	−7.8

[a] Calculated according to reference 32.

complexes and that the calculated values for all compounds use interatomic parameters for the fully solvated forms of the compounds, whereas the magnetic susceptibility measurements were performed on desolvated samples.

Conclusions

A trinuclear acetate-containing ferric complex has proved a useful precursor for a series of polynuclear complexes of *o*-dioxolene ligands that display a variety of nuclearities and structural architectures. Although a distorted monovacant cubane is a structural fragment common to a number of these complexes, the substituents on the *o*-dioxolene ligands clearly play a significant structure directing role, with steric crowding apparently preventing the formation of complexes of nuclearity higher than four when the *o*-dioxolene ligands are substituted with bulky *tert*-butyl groups. The redox state of the *o*-dioxolene ligands also affects the structure of the complexes, with all of the catecholate ligands employed observed to bridge the metal centers, regardless of the substituents. However, the smaller electron density on the semiquinonate form of the ligand appears to lead to a preference for binding in a non-bridging capacity.

Although the iron centers in these complexes are redox active, electrochemical studies indicated that the richest redox behavior is associated with the *o*-dioxolene ligands. Of particular interest in this regard are the three tetranuclear complexes, which despite their possession of a common structural core, differ in the number and redox state of the *o*-dioxolene ligands. A detailed investigation of the chemical and electrochemical one-electron oxidation of one of these complexes revealed the initial formation in solution of a kinetic product, with apparent retention of the structure, followed by structural rearrangement to a thermodynamic product, which could be isolated in the solid state and structurally characterized. This oxidation-induced structural rearrangement involves breaking and reforming a number of metal−ligand bonds and appears to be driven by the preference of the semiquinone ligand, obtained from the oxidation of a catechol ligand, to bind in a non-bridging mode.

Magnetochemical studies of the compounds obtained indicate behavior dominated by antiferromagnetic pairwise exchange interactions between the ferric centers. The magnetic susceptibility data for the single complex that possesses a semiquinone ligand suggest a very strong antiferromagnetic interaction between the radical ligand and the iron center to which it is bound. The coupling constants determined from fitting or simulating the thermal variation of the magnetic susceptibility for the family of complexes are consistent with magnetostructural correlations that have been reported previously for alkoxo-bridged ferric complexes.

Acknowledgment. We thank the Australian Research Council for financial support.

Supporting Information Available: X-ray crystallographic files in CIF format for **2**·Et_2O, **3**·CH_2Cl_2·Et_2O, **4**·$4CH_2Cl_2$, **5a**·$5CH_2Cl_2$, **6**·$4C_7H_8$·C_6H_{14}, **7**·$4Et_2O$, and **8a**·$2CH_2Cl_2$. Infrared spectra for compounds **5a** and **6**. Plot of $\chi_M T$ and χ_M vs T for **8a**. Plots of $M/N\beta$ vs H/T for compounds **3**, **4**, **5a**, **6**, **7**, and **8a**. This material is available free of charge via the Internet at http://pubs.acs.org.